BUREAU OF — RECLAMATION

Evaporation from Lake Powell: In-situ Monitoring between 2018 and 2021

Technical Memorandum No. ENV-2023-007
Upper Colorado Basin Region

Mission Statements

The Department of the Interior (DOI) conserves and manages the Nation's natural resources and cultural heritage for the benefit and enjoyment of the American people, provides scientific and other information about natural resources and natural hazards to address societal challenges and create opportunities for the American people, and honors the Nation's trust responsibilities or special commitments to American Indians, Alaska Natives, and affiliated island communities to help them prosper.

The mission of the Bureau of Reclamation is to manage, develop, and protect water and related resources in an environmentally and economically sound manner in the interest of the American public.

Cover photo of Lake Powell and floating platform by Daniel Broman (2018).

Evaporation from Lake Powell: In-situ Monitoring between 2018 and 2021

Prepared: Kathleen D. Holman, Ph.D.
Meteorologist
Water Resources Engineering and Management Group, 86-68210

Prepared: Chris Pearson
Associate Research Scientist, Hydrology
Desert Research Institute

Prepared: Richard Jasoni, Ph.D.
Associate Research Scientist, Biology
Desert Research Institute

Prepared: Justin Huntington, Ph.D.
Research Professor, Hydrology
Desert Research Institute

Prepared: John Volk, Ph.D.
Assistant Research Scientist, Hydrologic Software Engineer
Desert Research Institute

Internal Peer Review: Lindsay Bearup, P.E., Ph.D.
Civil Engineer (Hydrologic)
Water Resources Engineering and Management Group, 86-68210

Executive Summary

This report presents hydrometeorological observations and estimates of reservoir evaporation from two monitoring locations at Lake Powell from November 2018 to December 2021. We compare evaporation estimates from two independent methods, aerodynamic mass transfer and eddy covariance, to provide updated reservoir evaporation estimates based on best available science and methodologies. The main objectives of this study are to:

- collect over water micrometeorological and water temperature data to estimate evaporation rates
- perform side-by-side comparisons of evaporation rates from eddy covariance and aerodynamic mass transfer techniques
- calibrate bulk mass transfer coefficient used in aerodynamic computations using eddy covariance estimates
- compare point evaporation estimates with estimates developed using gridded weather data
- investigate remotely sensed surface temperature and modeled climate datasets for better understanding and accounting of spatial and temporal variability in evaporation

These objectives are accomplished through in-situ hydrometeorological data collection using floating observation platforms as well as intensive data processing and intercomparison with gridded climate datasets, remote sensing observations, and previous estimates.

Monthly comparisons with previously reported evaporation estimates, including gross evaporation coefficients (Reclamation 1986), floating evaporation pan estimates (Reclamation 2021), and reference evapotranspiration, show significant differences in evaporation timing and magnitude relative to evaporation estimates produced by this study. Eddy covariance and aerodynamic evaporation estimates calculated in the current study are consistently lower and show more pronounced peak evaporation timing than previously reported evaporation values from Lake Powell. In addition to presenting results, this report highlights the differences and limitations of each method, makes recommendations for continued data collection, and outlines opportunities for operational monitoring with advanced climate and remote sensing datasets.

Aerodynamic mass transfer evaporation estimates were highly correlated with eddy covariance evaporation estimates at both monitoring locations but were consistently biased low at monthly and annual timesteps. Bias is likely related to seasonal patterns of wind speed, temperature, vapor pressure deficit, and near surface atmospheric stability. Calibration of the aerodynamic mass transfer coefficient using eddy covariance estimates show similar seasonal patterns at both

sites identifying potential limitations with the application of Monin-Obukhov Similarity Theory in this study. Both methods capture reservoir heat storage impacts that shift peak evaporation timing to the late summer and fall relative to shallower systems and the annual solar energy cycle. Correction of eddy covariance evaporation estimates for wave-induced platform motion showed larger impacts at short timescales (sub-hourly to daily), however, longer-term evaporation totals (monthly to annual) were less impacted.

In-situ measurements of surface water skin temperature compare well with coincident lake surface temperature observations from Landsat 8 (average r-squared of 0.95 and bias of 7%). Comparisons of in-situ climate data with estimates from the National Weather Service Real-Time Mesoscale Analysis (RTMA) data product show good correlation and limited bias. Comparison of eddy covariance estimates with preliminary estimates from OpenET's Priestley-Taylor Jet Propulsion Laboratory (PTJPL) remote sensing model highlight the need to consider uncertainty in both forcing data and the scaling of instantaneous evaporation estimates derived at the time of satellite overpass to daily total estimates. Despite uncertainty in remote sensing model estimates, results demonstrate the potential for combination approaches based on gridded climate data and remote sensing to account for spatial differences related to climate and water temperature variability which may, in turn, lead to improved estimates of total reservoir evaporation. Future work will focus on model refinement and validation using in-situ observations collected during this study.

Table of Contents

List of Figures

List of Tables

List of Abbreviations

CFEP – Collison Floating Evaporation Pan
CNR4 – 4 Component Net Radiometer
CS225 – Campbell Scientific temperature string
DRI – Desert Research Institute
EC – Eddy Covariance
ETo – Grass Reference Evapotranspiration
ET –Evapotranspiration
IMU – Inertial Momentum Unit
IRGASON – Infrared Gas Analyzer (IRGA) and 3D Sonic (SON) anemometer
IRT – Infrared Thermometer
LEM – Lake Evaporation Model
LST – Land Surface Temperature
MAE – Mean Absolute Error
MI – Multiple Imputation
MICE – Multivariate Imputation by Chained Equations
MOST – Monin-Obukhov Similarity Theory
MST – Mountain Standard Time
NLDAS – North American Land Data Assimilation System
pmm – Predictive Mean Matching
PTJPL – Priestley-Taylor Jet Propulsion Laboratory
RH – Relative Humidity
RMSE – Root Mean Square Error
S&T – Science and Technology
UCRB – Upper Colorado River Basin
VPD – Vapor Pressure Difference

1 Introduction

1.1 Background

The Colorado River begins at the Continental Divide in the Rocky Mountains of Colorado, drains parts of seven different US states (Arizona, California, Colorado, Nevada, New Mexico, Utah, and Wyoming) and Mexico, and discharges into the Gulf of California (Christensen et al. 2004; Reclamation 2011). Nearly 40 million people living in those seven US states rely on the Colorado River and its tributaries for some or all municipal water needs (Reclamation 2021). Lake Powell, the second largest reservoir by capacity in the US, is formed by the flooding of Glen Canyon along the Arizona/Utah border by Glen Canyon Dam and acts to separate the Upper and Lower Basins (Figure 1). At full capacity, Lake Powell extends nearly 322 km (200 miles; USGS 2022) upstream of the dam.
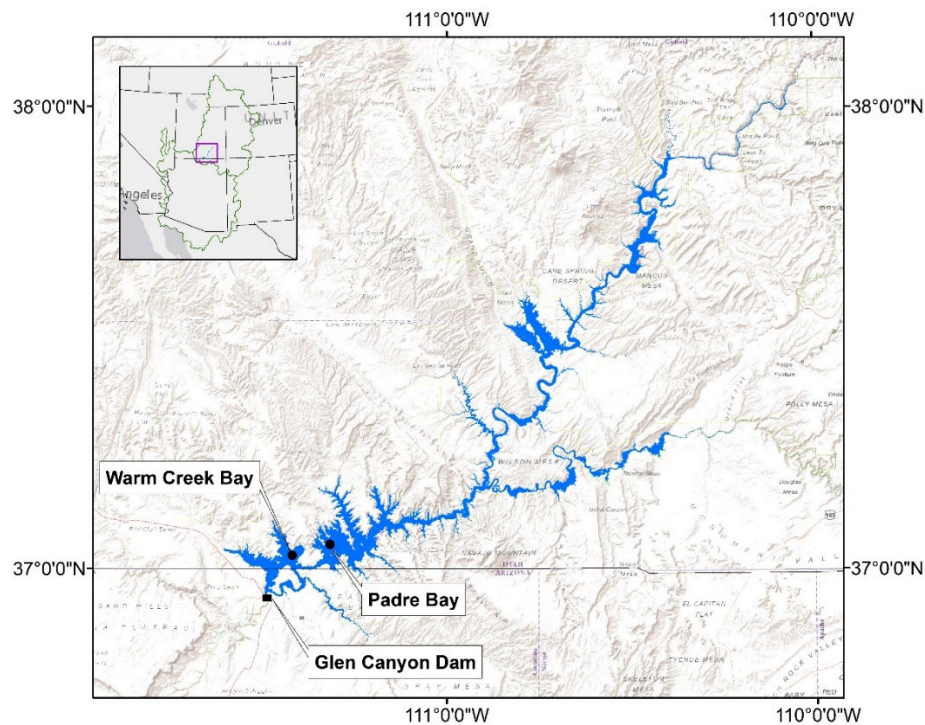
Figure 1—Map of Lake Powell, Glen Canyon Dam, and two floating platforms used to support updated evaporation estimates. Inset shows the location of the study area (purple rectangle) and Upper and Lower Colorado Basins (green polygons).

The National Park Service and the Bureau of Reclamation (Reclamation) manage the lands surrounding Lake Powell (USGS 2022). Climate in the region is described as arid. Maximum air temperatures often reach 37.7°C in summer months and less than 0°C in winter months. Typically, less than 254 mm (10 in) of precipitation fall each year. Streamflow into the reservoir is largely the result of snowmelt, which accumulates throughout the winter as snowpack in high-elevation regions of the Rocky Mountains (Reclamation 2021). While water levels have varied substantially throughout history (e.g., Figure 2 of USGS 2022), recent record-breaking minimums (Figure 2) have stressed hydropower generation and water deliveries. Improving estimates of water losses at Lake Powell is critically important now, as water managers across the seven basin states are making emergency releases to support water levels at Lake Powell and enacting drought contingency plans to manage the scarce resources available.
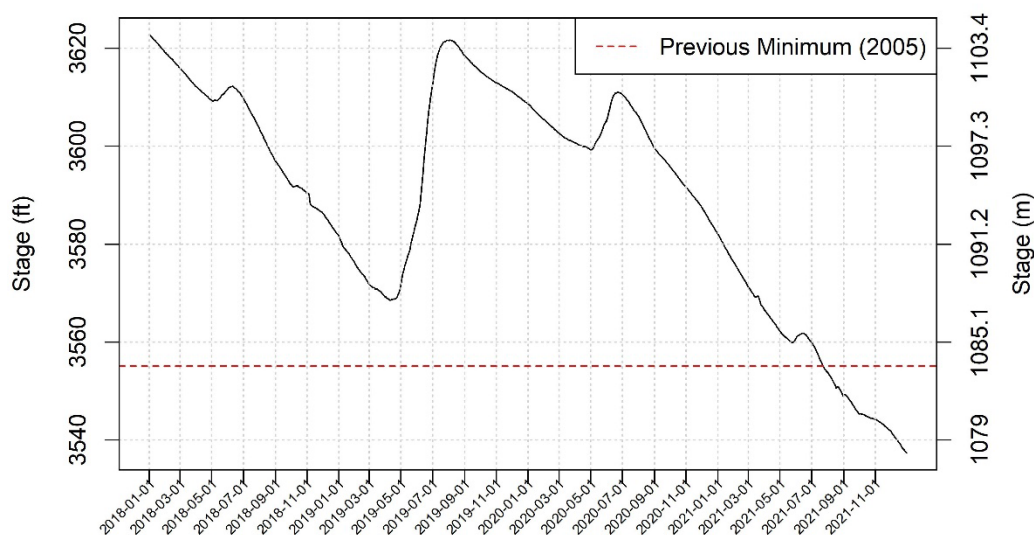
Figure 2—Time series of daily stage at Lake Powell between January 1, 2018, and December 31, 2021.

Modeling reservoirs and river systems throughout the Colorado River Basin is crucial for operations and planning activities. Reclamation employs three different RiverWare[TM] models to simulate conditions at short (up to 24 months), medium (up to 60 months), and long (multiple decades) time scales. The three RiverWare[TM] models use static monthly evaporation estimates for Lake Powell that are based on a report published by the Reclamation's Upper Colorado Basin Regional Office in the late 1980s (Reclamation 1986). Those estimates, which equal an annual loss of 1743.71 mm (68.65 in or 5.72 ft), are based on the mass transfer approach, where the transfer coefficient is a function of (static) fetch length.

Technical Memorandum No. ENV-2023-007
Evaporation from Lake Powell: In-situ Monitoring between 2018 and 2021

While estimates from Reclamation (1986) are used to support operational modeling efforts, alternative estimates exist. For example, La Rue (1925) estimated evaporation to be 1520 mm/yr (5 ft/yr). Clayton (2004, 2008) estimated evaporation from Lake Powell to be 1760 mm/yr (5.77 ft/yr). Huntington et al. (2015) estimated the mean annual 1950-1999 evaporation to be 1610 mm/yr (5.5 ft/yr). Myers (2013) conducted a water balance simulation and noted that reservoir evaporation and seepage losses were highly dependent on stage and surface area, and larger losses and changes in partitioning between evaporation and seepage could affect downstream allocations. Myers (2013) concluded that lowering reservoir storage could reduce evaporation and recover seepage losses up to 14.8 billion m^3 per year.

While alternative evaporation estimates exist for Lake Powell, none is based on the eddy covariance approach, and none estimate evaporative losses across the reservoir surface. Thus, the purpose of the current study is to develop updated estimates of evaporation from Lake Powell using research-grade technologies, while validating state-of-the-art gridded meteorological datasets and remote sensing techniques with in-situ observations recorded over water. The primary objectives are to:

- collect over-water micrometeorological and weather data to estimate evaporation rates via the eddy covariance (EC) and aerodynamic methods
- perform side-by-side comparisons of evaporation rates from the two measurement techniques (i.e., EC and aerodynamic)
- calibrate the bulk mass transfer coefficient used in aerodynamic computations
- compare point evaporation estimates with estimates developed using gridded weather data
- integrate remotely sensed surface temperature and modeled meteorological datasets for better understanding and accounting of spatial and temporal variability in evaporation

We accomplish the listed objectives by analyzing high frequency hydrometeorological observations recorded at two different locations on Lake Powell (see point callouts in Figure 3) between November 2018 and December 2021 and comparing over-water observations with estimates retrieved from gridded weather and remotely sensed datasets. While the focus of the current study is on observations recorded between 2018 and 2021, data collection at the two sites continues through the present. Observations and evaporation estimates based on data recorded after December 2021 will be summarized in a separate document.

1.2 Site Locations

To account for spatial variability in near-surface weather, in-water processes, and evaporation across Lake Powell, we are collecting over-water observations using instrumentation installed on two different floating platforms. One platform is located in Padre Bay, while the second platform is located in Warm Creek Bay (Figure 3). These two locations were selected to minimize fetch contributions from surrounding land and are representative of a significant portion of lake surface area (i.e., large, deep bays versus narrow slot canyons). The two platforms are set up with identical instrumentation (see Section 1.3 and Figure 4).
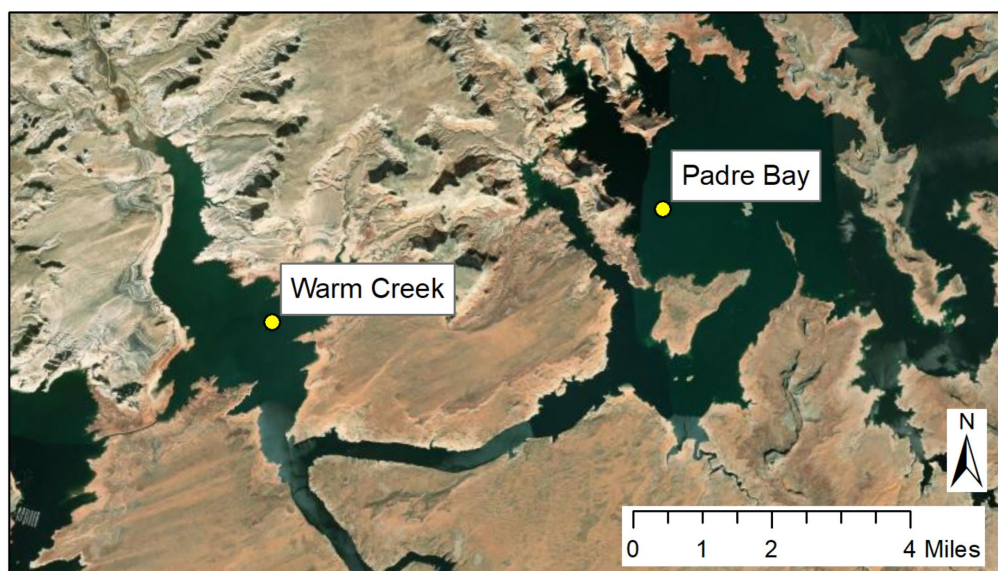
Figure 3—Location of Padre Bay and Warm Creek Bay monitoring platforms. Basemap satellite image valid November 17, 2018.

1.3 Instrumentation

The platforms deployed at Padre Bay and Warm Creek Bay (Figure 4) measure 2.4 m by 6 m (width by length). Each one is rigged with a counterweight anchor system that allows for vertical movement with reservoir stage changes, while limiting platform drift and rotation (yaw). Platforms include a suite of meteorological and water sensors for monitoring lake and atmosphere conditions. Instruments monitor air and water temperature, relative humidity, wind speed and direction, barometric pressure, and incoming and outgoing shortwave and longwave radiation (Table 1.1). In addition, each site is equipped with an all-in-one measuring device known as an IRGASON, which uses an infrared gas analyzer (IRGA) co-located with a three-dimensional (3D) sonic (SON)

anemometer to collect high-frequency (10-Hz or 10 measurements per second) atmospheric moisture and wind observations in support of the EC method. The other sensors generally support the aerodynamic method. Each platform is also outfitted with an inertial measurement unit (IMU) for monitoring IRGASON sensor head orientation and 3D accelerations related to platform motion. Data were collected remotely in near-real time via communication with on-board cellular modems. All EC and IMU observations were measured and recorded at a frequency of 10 Hz. Non-eddy covariance meteorological data were measured at a 10-second sampling rate and averaged to 30 minutes (i.e., 30-minute average based on 10-second samples). Water temperature profile data were measured at a 10-second sampling rate and recorded at 10-minute averages (i.e., 10-minute average based on 10-second samples).

Figure 4—Photo of instruments installed on platform floating in Padre Bay. The Warm Creek Bay platform is nearly identical.

Table 1.1—List of instruments installed at Padre Bay and Warm Creek Bay.

Sensor	Model	Vender	Method	Description	Sampling Rate	Recording Rate
Data Logger	CR6	Campbell Scientific	EC	Data acquisition for eddy covariance system	10 Hz	-
Co-Located Gas Analyzer and Sonic Anemometer	IRGASON	Campbell Scientific	EC	3D wind speed and magnitude; Water vapor content	10 Hz	10 Hz
Air Temperature	107 Probe	Campbell Scientific	EC	Eddy Covariance Air Temperature	10 second	30 min average
Inertial Motion Unit	3DM-GX5-25	LORD Microstrain	EC	EC Motion Correction	10 Hz	10 Hz
Rain Gauge	TE525WS-L	Campbell Scientific	EC; Ancillary analysis	EC QAQC	Pulse Count	30 min total
Barometer	CS106	Campbell Scientific	EC	Barometric pressure monitoring	10 second	30 min average
Data Logger	CR1000	Campbell Scientific	Aerodynamic	Data acquisition for meteorological and temperature sensors	10 second	-
Air Temp/RH	HMP155	Campbell Scientific	Aerodynamic	Air temp and RH monitoring	10 second	30 min average
Infrared Thermometer (IRT)	SI-111; SI-131	Campbell Scientific	Aerodynamic	Skin temperature monitoring at air/water interface	10 second	30 min average
Anemometer	Wind Monitor Marine Version (5106-10)	RM Young	Aerodynamic	2-m Wind speed and direction	10 second	30 min average
4-component Radiometer/Pyrgeometer	CNR4	Kipp and Zonen	Aerodynamic, EC	4-component Radiometer; IRT LWin correction; EC Gap-filling	10 second	30 min average
Water Temperature Profile	CS225	Campbell Scientific	Ancillary analysis;	Measurement depths (m): 0.5, 1, 2, 4, 6, 8, 10, 12.5, 15, 20	10 second	10 min average

1.3.1 Sensor Outages

Sensor performance and data collection were relatively steady throughout the three-year study period considering the harsh environment and remote nature of the collection sites. However, some data outages and sensor malfunctions related to data collection/transmission, sensor failure, and power supply issues did occur during the study period. Table 1.2 summarizes major outages resulting in data gaps longer than 48-hours. Planned outages related to sensor calibration and configuration typically lasted less than 48 hours and are not included in this summary. Details on outages associated with specific variables are further described in sections 1.3.1.1 and 1.3.1.2.

Table 1.2—List of major sensor outages.

Station	Date Range	Outage Description
Padre Bay	Dec-2018	Memory Card Failure; Miscellaneous EC Data Outages
	Nov-2018 to Mar-2019	IRT Programming Error
	Sept-2019 to Feb-2020	Temperature String Failure
	Jan-2021 to Nov-2021	Temperature String Failure
Warm Creek Bay	Dec-2018	Memory Card Failure; Miscellaneous EC Data Outages
	Nov-2018 to Mar-2019	IRT Programming Error
	Jun-2020 to Jul-2020	Temperature String Failure
	Aug-2020 to Oct-2020	Intermittent CNR4 Outages
	Nov-2021 to Dec-2021	Temperature String Failure

Multiple outages of the CS225 temperature string occurred throughout the study. Initial CS225 sensor spacing configurations utilized 20-m cables with 10 measurement nodes located at 0.5, 1, 2, 4, 6, 8, 10, 12.5, 15, 20 m below the water surface. During June 2020, the Warm Creek CS225 sensor suffered a complete failure and was replaced with a reserve cable in July 2020. The replacement cable was manufactured with a different sensor spacing than the original cable and included measurement nodes at 0.5, 5.5, 8, 10.5, 12.5, 14.5, 16.5, 18.5, 19.5, 20 m below the water surface. Future analyses that depend on these data will interpolate the improperly spaced observations to the initial spacing.

1.3.1.1 Skin Temperature Measurements

Skin temperature measurements are used to compute the saturated specific humidity at the water surface (q_{sat}), a necessary variable for the aerodynamic method. Continuous, accurate measurements of water surface skin temperature are difficult to obtain due to variable wave action (i.e., non-uniform surface) and contamination of the sensor view path by debris, such as dirt, spider webs, and insect nests (Reclamation 2021). The IRT sensor lens was cleaned as often as possible; however, service trips were limited to quarterly and biannual time

periods due to the remote nature of the sites and travel limitations. Identification of "bad" IRT data was further complicated by the fact that water surface skin temperature can be very similar to air temperature readings obtained when obstructions such as spider webs were present. All IRT skin temperature observations were compared to water temperature observations from the four-component radiometer outgoing pyrgeometer and readings from the 0.5-m water temperature measurement node. In general, IRT values generally agreed with surface temperature estimates based on outgoing longwave measurements throughout the three-year study period, tracking both seasonal and annual variability, as well as reservoir heat storage effects (Padre Bay: $R^2=0.94$, slope through zero=1.04; Warm Creek: $R^2=0.97$, slope through zero=1.04; comparison statistics based on all available 30-minute surface temperature data). However, issues related to platform interference in the outgoing longwave data were noted during data review and postprocessing (refer to section 1.3.1.2 for additional details).

The IRT sensor at Padre Bay was replaced with a narrower view path model (Apogee Model SI-131; 14° field of view) part way through the study due to failure of the initial sensor (Apogee Model SI-111; 22° field of view). Use of the narrow path sensor added additional noise to the skin temperature readings relative to the wider field of view model due to the decreased integration area and sensor sensitivity differences. All aerodynamic estimates were performed using 30-minute average IRT values in an effort to smooth shorter-term noise related to sensor differences. Comparison of IRT-based skin temperature measurements with surface water temperature based on outgoing longwave measurements were consistent at both study sites despite IRT view path differences.

1.3.1.2   Outgoing Shortwave and Longwave Measurements

Deployment of the four-component radiometer utilized an aluminum pipe boom extended out over the water surface approximately 1.83 m at a height of 1.5 m to measure both incoming and outgoing shortwave and longwave radiation. A bias in outgoing longwave data was discovered during review and during comparison with data collected by the IRT and 0.5-m water temperature node. We found this bias when comparing estimated skin temperature based on measured outgoing longwave radiation with IRT-based skin temperatures and water temperature measured at the 0.5 m node. Measurement differences varied with season, time of day (driven by solar radiation), and warming and cooling of the observation platform. This bias in outgoing observations was due to the wide view angle (approximately 150°) of the four-component radiometer and inclusion of the platform within the outgoing observations. Bias assessment and correction of outgoing longwave and shortwave measurements will be explored during future comparisons.

During March 2021, the four-component radiometer was extended further beyond the platform to 3.7 m from the platform edge to reduce the influence of the floating platform on outgoing observations. Water temperature estimates based on the outgoing longwave data collected after the boom extension show better agreement with temperature observations collected using the IRT (Padre Bay: R^2=0.95, slope through zero=1.03; Warm Creek: R^2=0.99, slope through zero=1.02; comparison statistics based on 30-minutes surface temperature data collected after March 2021). Despite the boom extension, influence of the platform remains unavoidable and is present to some extent in all outgoing radiation observations. To avoid biases related to the platform interface, only incoming radiation (i.e., shortwave and longwave) data were utilized during gap filling routines.

1.4 Water Levels

Throughout the study period, reservoir water levels varied drastically and even dropped below historical minimums (Figure 2). During initial deployment in November 2018, Padre Bay and Warm Creek Bay platforms were located in water that was approximately 43 m and 36 m deep, respectively. However, in December 2021, water levels at Lake Powell reached an all-time low level. Thus, the Padre Bay and Warm Creek Bay platforms in December 2021 were located in approximately 28 m and 21.3 m of water, respectively. Changes in water depth can influence evaporation rates through changes in heat stored within the water column. In addition, changes in reservoir depth also impact the distance between the floating platforms and the shoreline (Figure 5). This distance is particularly important when characterizing the flux footprint of the EC method. We considered water levels and distance from shore in flux footprints at both locations (see section 2.1.3).
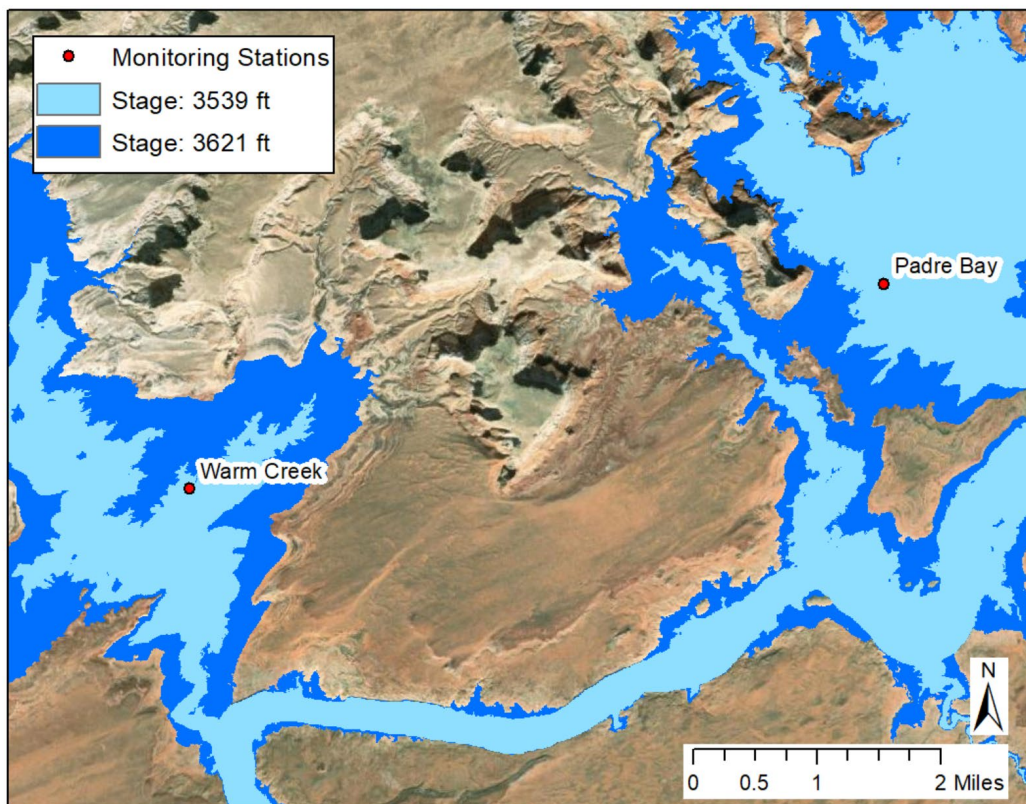
Figure 5—Spatial extent of water surface area at two discrete stage values based on bathymetry data obtained from Andrews et al. (2018). The maximum stage during this study was observed on August 3, 2019, while the minimum stage (at the time of this report) was observed on December 18, 2021. The land surface surrounding the water body is depicted by the satellite imagery base map.

1.5 Report Notes

Team members from the Desert Research Institute, Technical Service Center, and Page Field Office deployed the two floating platforms on November 7, 2018. The last batch of data analyzed for this report was retrieved on December 16, 2021. This is the primary study period included in the current study. Daily gap-filled estimates on November 7, 2018, and December 16, 2021, represent partial totals, along with monthly sums from November 2018 and December 2021. All variables are presented in International Standard of Units (SI), except for evaporation, which is shown graphically in SI units and in tabular form in SI and imperial units. We use the terms "evaporation estimates" and "evaporation totals" interchangeably, largely because all methods represent estimates.

The current study is organized as follows. In-situ methods used to develop evaporation estimates are summarized in chapter 2. Alternative evaporation estimates used for comparison's sake are summarized in chapter 3. Chapter 4 includes study results, with an emphasis on daily, monthly, and annual time scales. Finally, chapter 5 discusses study limitations, while chapter 6 summarizes the current report and next steps. Supporting methodological details, additional analyses, and high-frequency (e.g., 30-min) data are available in appendices.

2 Study Methods

A primary objective of the current study was to estimate evaporation from Lake Powell using two in-situ methods commonly discussed in the literature, specifically the EC and aerodynamic mass transfer methods. In this chapter, we discuss the details of each method as applied in the current study. We also discuss the methods used to estimate the flux source area and gap fill in-situ evaporation estimates.

2.1 Eddy Covariance

Turbulent airflow, also referred to as eddies, transfers energy and mass between the Earth's surface and the overlying atmosphere through turbulent exchange processes. The EC method is considered the most direct and defensible approach to quantify turbulent exchange, including water vapor and other trace gases (Baldocchi et al. 1988). Evaporation (i.e., positive latent heat flux) occurs when the concentration of water vapor in upward moving eddies exceeds the concentration of water vapor in downward moving eddies. Fluxes are measured by computing the covariance of a scalar (e.g., water vapor) and vertical wind speed. Following Baldocchi et al. (1988) and others, the water vapor flux density is calculated as the covariance of vertical wind speed and water vapor density, where both terms are instantaneous deviations from the time average. The latent heat flux can then be expressed as

$$LE = L_v \overline{w' q_v'}, \tag{1}$$

where L_v is the latent heat of vaporization, w' is the vertical component of wind speed, and q_v' is water vapor density. The prime symbols represent deviations from a time mean while the overbar denotes a time mean. To adequately measure these deviations, the EC method requires high-frequency observations of vertical wind speed and water vapor, typically on the order of 10 measurements per second (i.e., 10 Hz). These high-frequency observations must be post-processed and analyzed to develop useful estimates of evaporation. To efficiently process the large amount of 10-Hz data recorded at both sites we developed a workflow

shown in Figure 6. Additional details on these steps are provided in the sections below.

Figure 6—Schematic of workflow used to process 10 Hz eddy covariance data.

2.1.1 Platform Motion

The IRGASONs installed at Padre Bay and Warm Creek Bay are mounted to floating platforms. As a result, the 3D wind measurements recorded by the sonic anemometers were influenced by atmospheric motion in addition to platform motion induced from waves. To account for the additional motion of the platform, we installed an IMU with each IRGASON to record platform accelerations at the same rate as the IRGASON measurements (i.e., 10 Hz). We applied the methods of Miller et al. (2008) to remove platform motions from the observed 3D wind speed components at Padre Bay and Warm Creek Bay. Accounting for motion in the 3D wind field resulted in two sets of 10 Hz data files. The first set of data files included 3D wind speeds that were corrected for platform motion. The second set of data files included 3D wind speeds that were uncorrected (i.e., recorded observations). Maintaining two sets of data files allowed us to examine impacts of platform motion on evaporation totals. All results in the body of the report represent motion-corrected evaporation estimates unless otherwise stated.

2.1.2 EasyFlux PC

The EasyFlux PC® software package (Campbell, 2017) was used to process 10-Hz measurements using both corrected and uncorrected wind speeds. We applied standard filtering options and data corrections (described below) from EasyFlux PC to the 10-Hz observations to produce 30-minute average estimates. The EasyFlux PC software removed wind speed and water vapor observations when there were non-zero sonic diagnostic flags and non-zero gas analyzer diagnostics reported, respectively (Campbell Scientific, 2022). Implausible water vapor observations were also removed via a de-spiking algorithm. More specifically, 10-Hz observations were de-spiked using the method of Vickers and Mahrt (1997), with the maximum consecutive outlier threshold set to 3, the plausibility range set to 3.5, and the accepted spike percentage set to 1%. We applied the double coordinate rotation of Tanner and Thurtell (1969) to winds recorded by the sonic anemometer (for both motion-corrected and motion-uncorrected winds). Low-pass filtering effects were corrected by applying spectral methods of Massman (2000, 2001). Finally, we corrected for density variations using the methods of Webb et al. (1980).

12

2.1.3   Source Area of Flux

Turbulent flux measurements are representative of some geographic area (i.e., spatial domain) upstream of the measurement location. This geographic area is sometimes referred to as the source area, fetch, or flux footprint, and depends on factors such as measurement height, surface roughness, and atmospheric stability. In this section, we present two footprint analyses; the first footprint analysis is based on output from the Campbell Scientific software, EasyFlux PC, and is based on a combination of the Kljun (Kljun et al. 2015) and Kormann and Meixner (Kormann and Meixner, 2001) models. The second footprint analysis is based on a 2D implementation of the Kljun et al. (2004) model (Kljun et al., 2015). The remaining sections describe these results.

2.1.3.1   Point Footprint

During each averaging period considered in EasyFlux PC (i.e., 30-minute window), the software computed an upwind flux distance (i.e., distance upwind of sensor contributing to estimated flux) using the Kljun et al. (2004) model. According to Kljun et al. (2015), flux footprint models describe the spatial extent and orientation of the surface area that contributes to a turbulent flux measurement at a specific point in time under certain atmospheric conditions and specified surface characteristics. For reservoir evaporation, a flux footprint describes the distance upwind of the EC equipment contributing to the flux. These models have become a standard analysis metric in many studies.

According to the EasyFlux PC manual (Campbell Scientific, 2020), the Kljun flux footprint model is used at every time step when appropriate conditions are met. If the appropriate conditions are not met, the Kormann and Meixner (2001) flux footprint model was used. Output from EasyFlux PC indicated which flux footprint model was used at each timestep (0=Kljun, 1=Kormann and Meixner). According to output from Padre Bay, the Kormann and Meixner model was used approximately 74% of the time during the study period. At Warm Creek Bay, the Kormann and Meixner model was used approximately 72% of the study period.

Results in Figure 7 show the distribution of upwind distances that contributed to a given fraction of the estimated evaporative flux based on 30-minute data recorded at each platform. At Padre Bay, the median upwind distance that contributed to 90% of the evaporative flux was 191 m. The median upwind distance that contributed to 90% of the evaporative flux at Warm Creek Bay was slightly lower at 135 m. Differences in upwind distances contributing to the total flux at each platform may have differed due to differences in wind conditions between the locations. These flux footprints are notably smaller than flux footprints cited in other EC studies (e.g., Blanken et al. 2012). While this was an intentional aspect of the study design (to limit flux contamination by surrounding land), there may be implications for the representativeness of these evaporative estimates across the remainder of the reservoir.
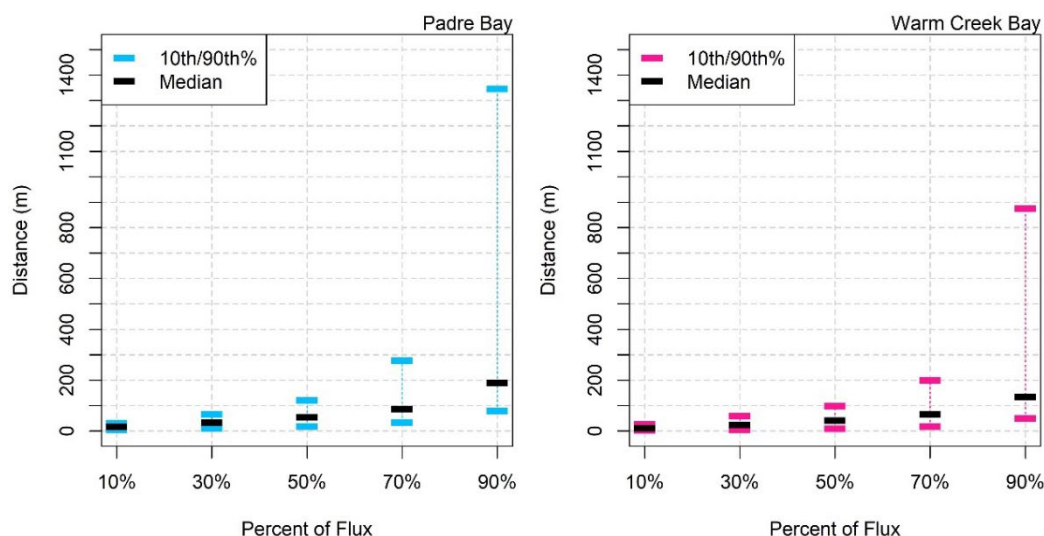
Figure 7—Upstream distance (m) contributing to each percentage of total flux valid at (left) Padre Bay and (right) Warm Creek Bay during the study period.

2.1.3.2 Spatial Footprint

Land contamination (flux values that originate from land surface and not water surface) within the flux source area is a concern for evaporation estimates at Lake Powell due to the relatively close distance to land, and water levels that varied throughout the year and have reached record low levels near the end of the study period (see section 1.4 on reservoir water levels). To avoid land contamination in EC evaporation estimates, we implemented the 2D physically based Kljun et al. (2015) flux footprint prediction model to estimate upwind source areas. Half-hourly footprint predictions were compared against daily estimates of land and water surface coverage over a domain centered around each platform. The location of the shoreline within each domain was adjusted based on daily water level measurements and bathymetry data obtained from Andrews et al. (2018). Daily water level information was used to develop land versus water masks based on lake digital elevation model (DEM) information. Final daily land mask layers were resampled to the flux footprint resolution using bilinear interpolation.

The Kljun et al. (2015) model used half-hourly variables including wind speed and direction, friction velocity, standard deviation of lateral wind velocity, and Monin-Obukhov length computed by EasyFlux PC. Other input parameters were estimated or assumed: planetary boundary layer height was assumed to be 2000 m and zero-plane displacement and roughness length were assumed to be 0 m due to the relatively smooth open water surface. The boundary layer height assumption was reasonable for unstable conditions, though sensitivity tests (not shown) indicated that the Kljun et al. (2015) model was insensitive to this parameter likely due to the relatively low wind-measurement heights. We also assumed that

14

small increases in roughness length and zero-plane displacement due to waves would have small impacts on the flux footprints. Lastly, we used a 3-m discretized 1200-m square grid for the footprint estimation and clipped the final footprints to only include the top 90% of pixels or 90% of the source area.

After intersecting half-hourly footprints with daily land exposure, we found that neither location recorded a significant contribution to the flux footprint originating over land (see Table 2.1). Small levels of contamination (fraction of 0.01 or less) were found but were rare. We tested using different fractional thresholds such as 0.05 or 0.0 (not shown). Annual evaporation totals were minimally affected by the change. As a result, we decided to use a strict threshold where 30-min values impacted by any amount of land contamination (i.e., fraction > 0.0) were removed and gap filled. At Padre Bay, we removed 40 30-min observations. At Warm Creek Bay, we removed 287 30-min observations, most of which occurred in the second half of 2021 when water levels were at record lows.

Table 2.1—Number of 30-minute evaporation rates impacted by land contamination. There are 52,128 possible 30-minute observations over the full period of record.

Fraction of Land Contamination	Number of 30-Minute Observations	
	Padre Bay	**Warm Creek Bay**
0.10	0	2
0.05	0	11
0.01	19	89
>0.0	40	287

2.1.4 Additional EC Quality Control

Additional processing of 30-minute data was required after running observations through EasyFlux PC. We removed 30-minute average evaporation estimates during periods of precipitation. Specifically, if tipping buckets at Padre Bay or Warm Creek Bay recorded precipitation greater than 0 mm, the corresponding 30-minute average evaporation total was removed. We also removed evaporation estimates during periods when the wind measurements were impacted by the presence of the IRGASON. This impact occurred when the horizontal wind direction was ±10° from behind the IRGASON instrument (Campbell Scientific, 2020). At Padre Bay, the back of the IRGASON was oriented to 337º. Thus, evaporation observations from times when the wind direction was from 327° to 347°, were set to missing. Similarly, at Warm Creek Bay, the back of the IRGASON was oriented to 324°. During wind directions of 314° to 334°, evaporation estimates were set to missing. Finally, we manually removed evaporation estimates during periods of time when the water vapor signal strength was below 0.7 at each station separately. The measures were applied to 30-minute data in addition to the default measures in EasyFlux PC and the flux footprint

criteria discussed above. We retained all other evaporation values. The number of data gaps at each site for each method is summarized in section 2.3.

2.2 Aerodynamic Mass-Transfer Method

In addition to the EC method, we applied an aerodynamic mass transfer approach to over-water meteorological and surface water temperature observations to estimate evaporation. The aerodynamic approach is based on Dalton's Law, where the evaporative flux is driven by the difference in vapor pressure between the saturated water surface and the air above. The general form of the aerodynamic equation is

$$E = \rho_{mair} C_E u (q_{sat} - q_2), \qquad (2)$$

where E is evaporation (mm t_{step}^{-1}), ρ_{mair} is the density of moist air (kg m^{-3}), C_E is the bulk transfer coefficient, u is the windspeed at 2 m (m s^{-1}), q_2 is the specific humidity at 2 m about the surface (kg kg^{-1}), and q_{sat} is the saturated specific humidity at the water surface. C_E values were based on Monin-Obukhov Similarity Theory (MOST) following equations developed by Brutsaert (1982). A detailed description of the aerodynamic method and MOST equations applied during this study can be found in Appendix 1.

The aerodynamic bulk mass transfer method offers an operational and cost-effective method for estimating reservoir evaporation when more direct estimates (e.g., eddy covariance) are difficult to obtain or are unavailable (Brutsaert, 2005; Quinn, 1979). Air temperature, relative humidity, barometric pressure, and windspeed were measured at 2 m above the water surface. Surface water temperature (i.e., "skin temperature") was measured using an infrared thermometer (IRT) boomed out and angled away from the measurement platform at the water surface. Corrections of IRT skin temperatures observations for the emissivity of water and impacts of incoming longwave radiation were performed according to methods outlined by Apogee Instruments (see Appendix 1 for detailed description of skin temperature corrections). IRT temperature estimates were computed assuming a constant water emissivity of 0.97 (Mohseni 1999; Lenters 2005). All aerodynamic meteorological and water temperature measurements were taken using a 10-second sampling rate and averaged to 30-minute values. Gap filling procedures for all 30-minute meteorological data is described below in section 2.3.

16

2.2.1   Manual Quality Control

All 30-minute observations used to support the aerodynamic method were manually reviewed and filtered during post-processing to remove data spikes, flat lines, and obvious out-of-range values related to sensor failures or electronic shortages. In general, bad values were assessed relative to observations taken before and after the suspect value as well as comparison to redundant measurement made by other sensors (e.g., propeller anemometer windspeed versus sonic anemometer windspeed or HMP-155 relative humidity versus IRGASON water vapor content). Additional screening was done to remove observations impacted by maintenance trips. Post-processing was completed using custom python-based plotting. All gap-filling procedures and evaporation calculations for the aerodynamic method were performed on the cleaned datasets. The number of data gaps at each site for each method is summarized in section 2.3.

2.3 Gap Filling

Gaps in high-frequency evaporation data occur for a number of reasons including system maintenance, power failures, equipment malfunctions, animal disturbances, weather events, and quality control measures (e.g., land contamination from wind direction, among others). Missing data can make it difficult to estimate seasonal or annual evaporation totals, establish relationships with climatic variables, and validate alternative modeling approaches (Hui et al., 2004). Consequently, most studies utilize some type of gap-filling algorithm to replace missing observations. Common approaches for gap filling evaporation data include mean replacement (i.e., using an average of observed values), interpolation and extrapolation, and regression analysis (i.e., predicting a missing value using a regression equation developed between said variable and other variables), among others (Hui et al. 2004). Although multiple methods exist, no standard method has been widely accepted (Alavi et al., 2006). The percent of missing values at each location for each method is shown in Table 2.2.

Table 2.2—Percent of 30-minute evaporation time series (N=52,128) set to missing.

Location	Method	Percent Missing 30-Min Evaporation Values
Padre Bay	EC Motion Uncorrected	15%
	EC Motion Corrected	15%
	Aerodynamic	12%
Warm Creek Bay	EC Motion Uncorrected	18%
	EC Motion Corrected	18%
	Aerodynamic	13%

In this study, data gaps in 30-minute latent heat flux estimated by the EC method and aerodynamic method were filled using the multiple imputation method (MI). MI is a general-purpose Monte Carlo technique that fills missing observations in a dataset while leaving observed values unchanged (Rubin 1987, 1996). There are three primary steps in MI: imputation, analysis, and pooling. During the imputation step, missing observations are replaced by sampling from distributions generated with the non-missing observations. This happens n times, representing n individual time series. Next, each of the n complete datasets is analyzed using normal statistical methods. Finally, in the pooling phase, results from the n complete datasets are combined to account for uncertainty in the imputed time series (Hui et al., 2004).

The MI method has been used in many studies to fill gaps in EC observations. For example, Hui et al. (2004) filled missing observations of net ecosystem carbon exchange, latent heat flux, and sensible heat flux recorded at three different FluxNet (fluxnet.org) sites using MI. Their results showed that annual estimates of net ecosystem exchange, latent heat flux, and sensible heat based on MI were comparable to other common imputation methods. Xue et al. (2012) filled missing evapotranspiration observations recorded over a larch forest in eastern Siberia between 2003 and 2006 using a Bayesian version of MI. Solar radiation, wind speed, relative humidity, and soil water content were used as predictors. Yonemura et al. (2017) used MI methods to fill missing carbon dioxide fluxes observed over paddy fields during a single fallow season. One suggested benefit of MI in filling EC gaps is the ability to retain noise in the data, which many traditional gap filling methods do not do (Aubinet et al. 2012).

We implemented a version of MI based on the Multiple Imputation Chained Equations (MICE) algorithm from van Buuren and Groothuis-Oudshoorn (2011) available through the R package, MICE. The specific univariate imputation model used to fill 30-minute average latent heat fluxes was predictive mean matching (pmm; Little 1988), one of the many imputation models built into MICE. The pmm method is a semi-parametric imputation approach, similar to the regression method that fills each missing value by randomly sampling an observed value whose regression-predicted value is closest to the regression-predicted value for the missing value from the simulated regression model (Heitjan and Little 1991; Schenker and Taylor 1996). According to van Buuren (2021), pmm imputations are restricted to observed values, and the method can preserve non-linear relations even if the structural part of the imputation model is wrong. van Buuren (2021) called pmm a good method overall. Each new round of imputation uses data points filled during the previous round of imputation (if one exists) to update relationships among variables.

Published studies have implemented a variety of predictor variables, suggesting that there is not a single set of "correct" predictors. van Buuren (2021), and

18

citations within, recommended using all available information to produce imputations that have minimal bias and maximal certainty. Thus, the number of predictors should be as large as possible. As a result, we included air temperature, air pressure, air density, water vapor density, rotated u-, v-, and w-components of the wind, wind direction, wind speed, skin temperature, incoming longwave radiation, and incoming shortwave radiation in the gap filling routine applied to EC data. We included air temperature, air pressure, relative humidity, wind speed, wind direction, skin temperature from the IRT sensor, incoming longwave radiation, and incoming shortwave radiation in the gap filling routine applied to aerodynamic data. We included skin temperature recorded from the CNR4 sensor to help fill long data gaps (i.e., gaps longer than two days) when the IRT sensor was down. Additional testing (not shown) indicated that adding the CNR4 skin temperature data as a predictor to the aerodynamic gap filling routine did not influence monthly and annual evaporation totals. We did not use evaporation estimates from one method as a predictor in the gap filling routine of the other method such that the two in-situ methods were completely independent. Default settings in the MICE algorithm result in five imputed time series that have zero missing observations. We averaged all five together to yield a single time series of evaporation for each location and method (where non-gap filled values remain unchanged).

Impacts of the gap-filling procedure on 30-minute and daily evaporation rates from the EC and aerodynamic methods are shown in Appendix 2. All evaporation results presented in the body of the report represent gap-filled estimates unless otherwise specified.

3 Additional Evaporation Estimates

We compare in-situ evaporation estimates with estimates from alternative sources that have historical context or relevance to other Reclamation projects. We include evaporation coefficients used to support modeling in the Colorado River Basin, evapotranspiration from a hypothetical grass surface, and estimates of evaporation from a floating pan located on Lake Powell that was funded through Reclamation's Science and Technology (S&T) Program. Additional details about each method are discussed below.

3.1 Gross Evaporation Coefficients

Reclamation employs three different RiverWare$^{\text{TM}}$ models to support planning and operations decision making in the Colorado River Basin. The models, which vary as a function of outlook duration, must represent the physical system, along with the legal constraints associated with water law in the basin. The three models simulate the movement and storage of water through river reaches, reservoirs, canals, and other infrastructure, while also accounting for water withdrawals, gains, and losses (Payton et al. 2020). The models are run at a monthly timestep, where Lake Powell evaporation rates are set to the static, monthly values shown in Figure 8 and described in Reclamation (1986). In this static dataset, peak evaporation rates always occur during July, with August and September second and third, respectively.
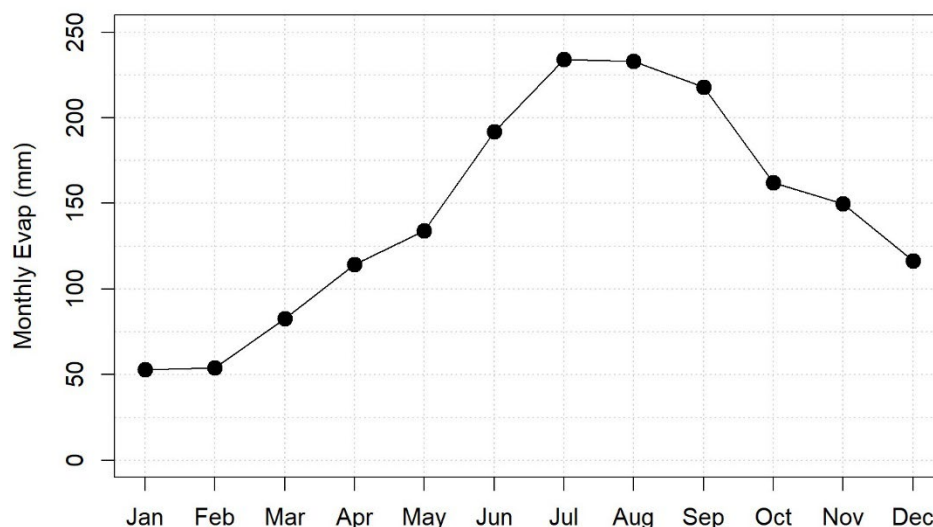
Figure 8—Lake Powell average monthly evaporation (mm) used in three models to simulate the Colorado River Basin system (Clayton 2008).

Because monthly evaporation rates applied to the surface area of Lake Powell are chosen to be constant, inter-annual variability in evaporation rate (i.e., year-to-year variations) is assumed to be zero. The annual evaporation rate is always 1744 mm (68.65 in or 5.72 ft). Volumetric losses of evaporation, however, do vary as a function of reservoir surface area, and in that sense some interannual variability in total evaporation is captured.

This dataset is often referred to as "coefficients" in historical reports, though the term "totals" is likely more appropriate. We retain the naming convention of this dataset in the current report to remain consistent with other historical documentation.

3.2 ASCE Reference Evapotranspiration

To demonstrate the influence of heat storage and differences between land and open-water evaporative flux, we calculated daily grass reference evapotranspiration (ETo) using the standardized Penman-Monteith equation of the American Society of Civil Engineers (ASCE-PM; ASCE-EWRI, 2005), which does not explicitly account for the effects of heat storage in the water column. ETo represents evapotranspiration from a clipped grass under well-watered and ideal conditions and is commonly used as a benchmark reference for evaporation and evapotranspiration estimates throughout the world. ASCE ETo is the preferred method for estimating agricultural crop and landscape water use. Comparison of ASCE ETo with open-water estimates from this study provides a basis to assess the influence of heat storage processes and understand historical and future responses to variable weather, climate, and atmospheric evaporative demand.

The daily ASCE-PM ETo equation was forced with in-situ measurements of air temperature, relative humidity, incoming shortwave radiation, and wind speed recorded at each platform separately. All calculations were performed with the Python RefET library. The Python RefET library was validated against the Ref-ET Software developed by the University of Idaho (Allen, 1992). Missing daily data were gap filled using the MI approach described above, where predictor variables include the same list of variables used to force the ETo equation. A full data logger outage occurred at Warm Creek Bay between November 3 and November 21, 2021. Rather than gap filling this period with no available predictor data, we simply replaced missing values of ETo at Warm Creek Bay with ETo estimates from Padre Bay.

3.3 Collison Floating Evaporation Pan

Reclamation's S&T Program funded a multi-year study (project ID 8119) to deploy a Collison Floating Evaporation Pan (CFEP) on Lake Powell between 2018 and 2020 (Reclamation, 2021). The floating pan consists of an interior evaporation pan 0.61 m (2 feet) deep and 2.44 m (8 feet) in diameter surrounded by reservoir water and a vertical outer wave guard that is 0.61 m (2 feet) deep and 6.1 m (20 feet) in diameter (Reclamation 2021). Figure 9 shows an image of the CFEP at Warm Creek Bay, which has been attached to this floating platform throughout the entire study period. A series of instruments are attached to the outer wave guard, and a cell modem allows for remote, real-time access of data. See Reclamation (2021) for the full list of observed variables.

Figure 9—Collison Floating Evaporation Pan attached to the floating platform in Warm Creek Bay. Figure from Reclamation (2021).

We compared CFEP evaporation estimates to EC and aerodynamic estimates at the Warm Creek Bay site between May 7, 2019, and April 30, 2020, when all methods include valid data. Since the CFEP study was funded through a different mechanism (e.g., a proposal selected for funding in the Science and Technology Program), the study was completed independently of the current study, and the data are presented without further discussion. See Collison (2019) for addition details on the CFEP method and Reclamation (2021) for additional information on the CFEP instruments and results specific to Lake Powell.

4 Study Results

The results section is organized as follows. First, we present in-situ evaporation estimates at daily, monthly, and annual time scales from the two locations. We compare in-situ estimates to estimates from the various alternative methods. Evaporation estimates at the 30-minute time scale are shown in Appendix 2. Next, we show results from two different method used to calibrate the mass transfer coefficient employed in the aerodynamic method. Finally, we present evaporation estimates from gridded meteorological and remote sensing applications.

4.1 In-Situ Evaporation Estimates

4.1.1 Daily Time Scale

Figure 10 shows daily evaporation estimates from Padre Bay and Warm Creek Bay based on the EC method. The time series of daily totals from both locations show a clear seasonal cycle with minimum values observed during late winter and early spring (e.g., February and March) and relative maximum values observed during late summer and early fall (e.g., August and September) at both locations. Daily totals from the EC method range from near 0 to almost 16 mm at both locations. The correlation (also referred to as r) between the two EC time series is 0.91. Daily differences between the two locations range from approximately -5.5 mm to +5.5 mm (Padre Bay minus Warm Creek Bay; middle panel of Figure 10), where the average daily total evaporation is 3.6 mm and 3.2 mm at Padre Bay and Warm Creek Bay, respectively, over the study period. The bottom panel of Figure 10 summarizes daily differences computed as a percentage of daily Padre Bay totals by month of year (statistics for each month are computed separately over the full study period) via a box and whisker plot. Results in this panel indicate that median daily percent differences between the two locations peak during the cool season, specifically November through January, with a peak median monthly difference of 22%. Small differences in average daily totals between the two locations grow with increasing duration such that the average monthly evaporation total over the study period is 107 mm and 96 mm at Padre Bay and Warm Creek Bay, respectively.
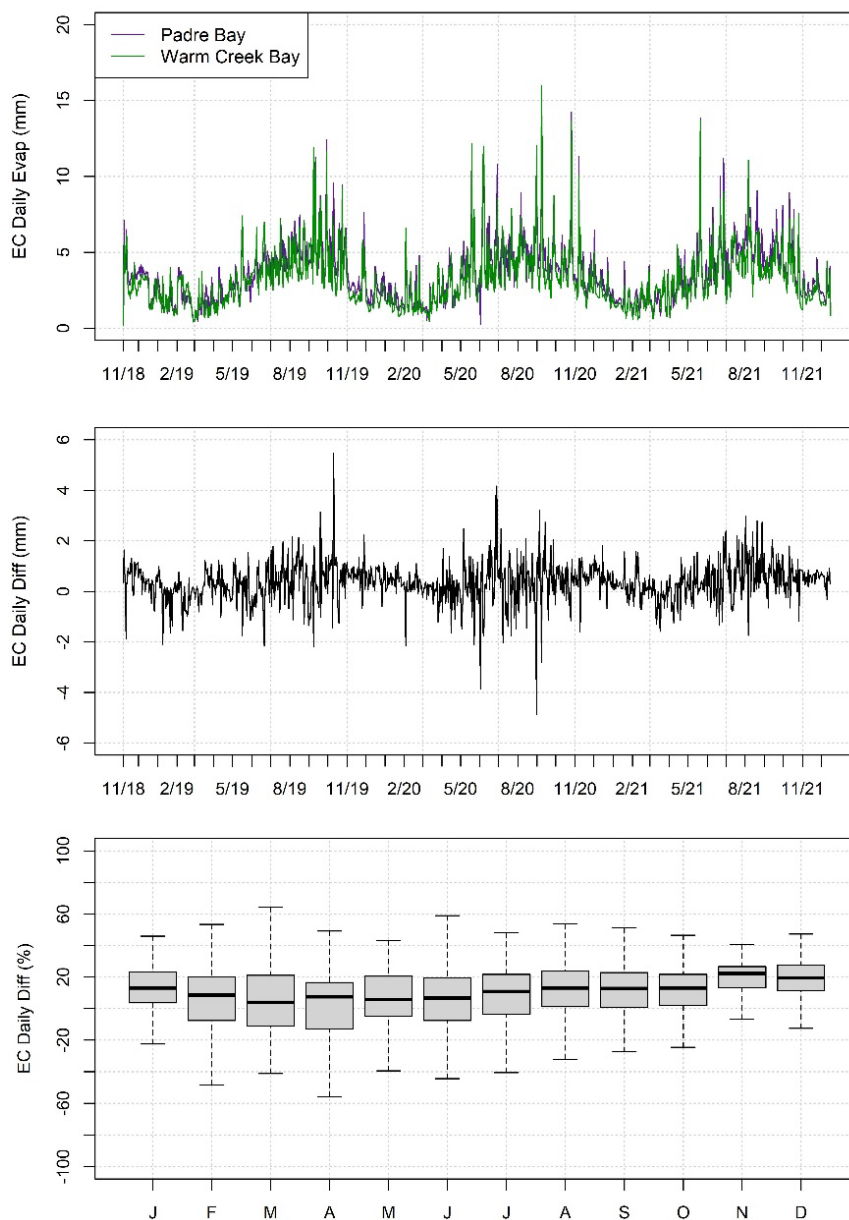
Figure 10—(top) Time series of daily EC evaporation totals (mm) at Padre Bay and Warm Creek Bay. (middle) Time series of daily EC totals from Padre Bay minus daily EC totals from Warm Creek Bay (mm). (bottom) Box and whisker plot of daily differences between Padre Bay and Warm Creek Bay expressed as a percent of daily totals at Padre Bay for each month of year over the full study period. Thick horizontal lines represent the monthly median. Boxes extend to the 25th and 75th percentiles. Whiskers extend to 1.5 times the interquartile range.

Daily aerodynamic evaporation time series from the two floating platforms are shown in Figure 11. As with EC estimates, we see that these time series are characterized by a strong seasonal cycle with daily maximums during the warm season and minimums during the cool season. The correlation between the two aerodynamic time series is 0.91. Absolute differences between the time series (middle panel of Figure 11) are similar in magnitude to differences observed with the EC method, namely -4 to +3.5 mm per day. Monthly median percent differences between the aerodynamic time series (bottom panel of Figure 11) are largest between October and February and exceed 30%. Thus, differences between the two sites are larger with the aerodynamic approach than EC approach.
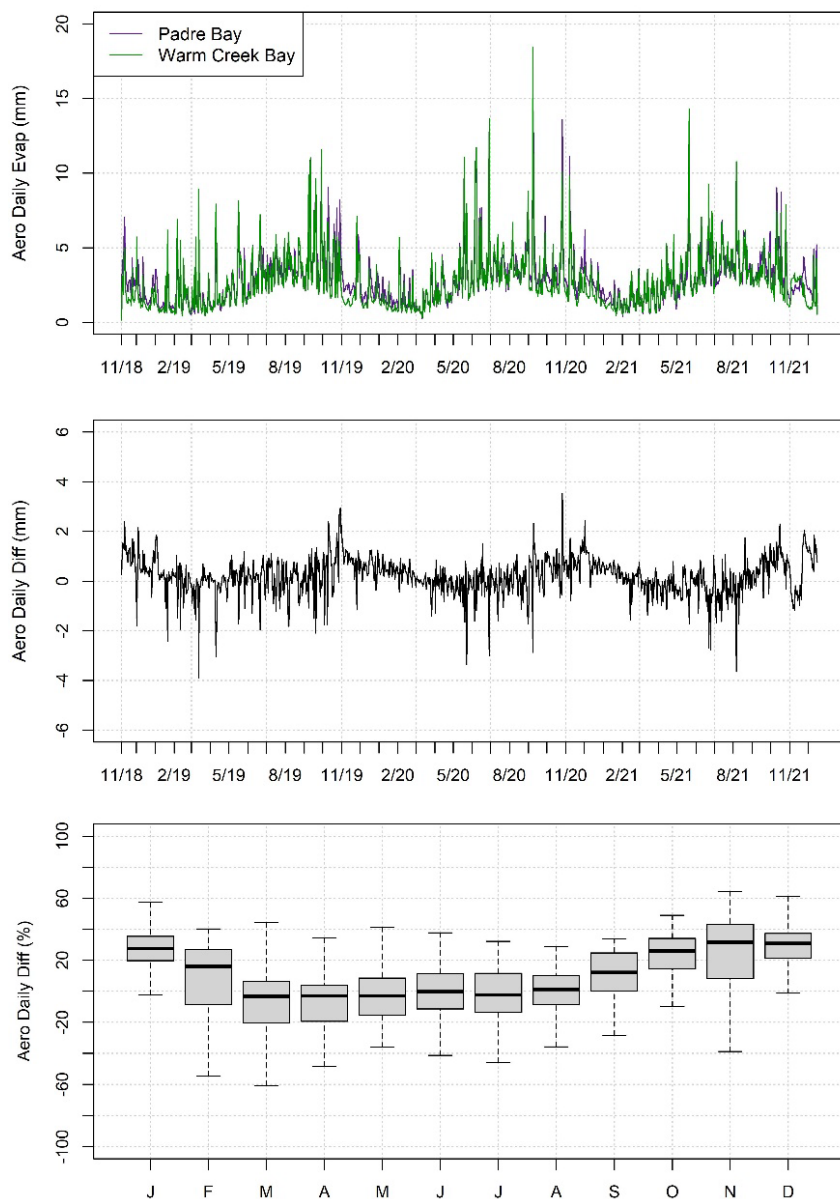
Figure 11—Same as Figure 10 except based on the aerodynamic approach.

Differences between the two in-situ methods are illustrated in Figure 12. The top panel shows time series of daily differences at the two locations (EC minus aerodynamic). At Padre Bay, daily differences between the methods range from -2.5 to +4.3 mm. Average daily total evaporation from the aerodynamic method at Padre Bay is 2.9 mm (compared to the 3.6 mm average daily total from EC). At Warm Creek Bay, daily differences between the two methods range from -6 to 3.5 mm, where average daily total evaporation from the aerodynamic method is 2.7 mm over the study period (compared to the 3.2 mm average daily total from EC).

26

Scatterplots in the bottom two panels of Figure 12 show the relationship between daily EC evaporation totals and daily aerodynamic evaporation totals at the two locations separately. Correlations between the two daily datasets are 0.91 and 0.89 at Padre Bay and Warm Creek Bay, respectively. The slope of a linear regression model fit to EC data predicted using aerodynamic data assuming a y-intercept of 0 (also referred to as slope through origin) is also shown in each panel of Figure 12. The slope through the origin is sometimes used as a metric for bias relative to the x-axis variable (e.g., Melton et al. 2021). In both panels, we see that the slope is greater than 1, indicating that daily EC totals generally exceed daily aerodynamic totals by 17% and 9% at Padre Bay and Warm Creek Bay, respectively. This finding suggests a general negative bias with the MOST-derived aerodynamic estimates.
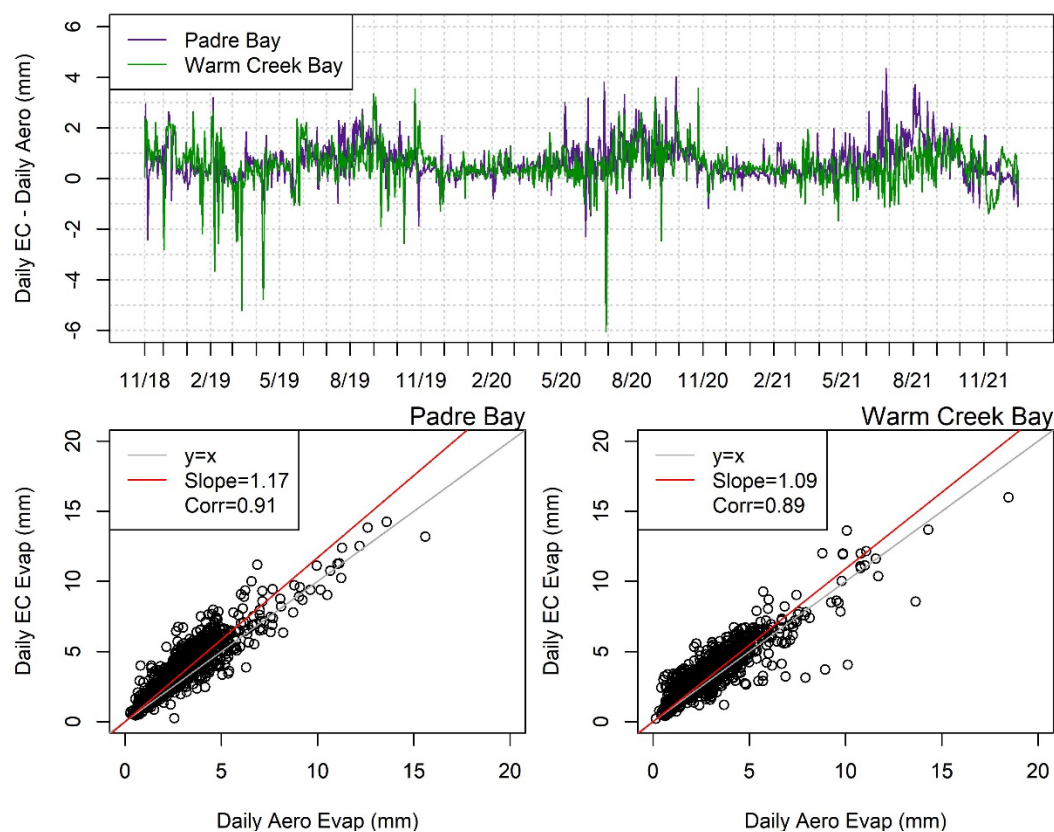
Figure 12—(top) Time series of daily EC evaporation totals minus daily aerodynamic evaporation totals at Padre Bay and Warm Creek Bay. (bottom) Scatterplots of daily EC evaporation totals (mm) versus daily aerodynamic totals (mm) at (left) Padre Bay and (right) Warm Creek Bay. Slope values represent the slope of a linear model when forced through the intercept (0,0). Correlation values are also listed.

4.1.2   Monthly Time Scale

Location and method comparisons at the monthly time step are shown in Figure 13. Results in the top two panels (a and b) of Figure 13 indicate that monthly evaporation totals from Padre Bay are generally larger than corresponding totals from Warm Creek Bay based on the EC and aerodynamic methods (11% and 5%, respectively). In absolute values, this equates to an average difference of 10.6 mm (0.42 in) between EC estimates at Padre Bay and Warm Creek Bay, where Padre Bay is larger. For aerodynamic totals, Padre Bay is on average 6.1 mm (0.24 in) greater than Warm Creek Bay.
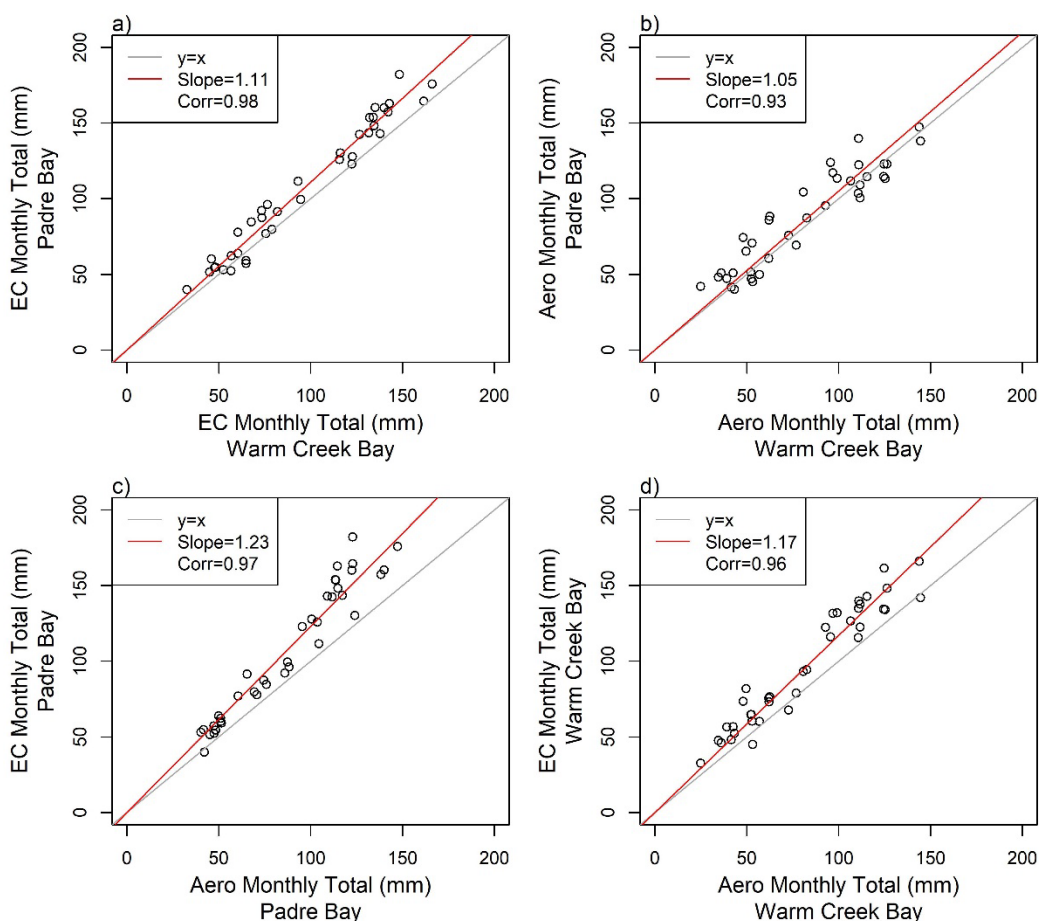
Figure 13—Scatterplots of monthly evaporation totals (mm): a) EC at Padre Bay versus EC at Warm Creek Bay, b) aerodynamic at Padre Bay versus aerodynamic at Warm Creek Bay, c) EC at Padre Bay versus aerodynamic at Padre Bay, and d) EC at Warm Creek Bay versus aerodynamic at Warm Creek Bay. Slope values represent the slope of a linear model when forced through the intercept (0,0). Correlation values are also listed.

Results in the bottom two panels of Figure 13 reflect differences between the two estimation methods. Monthly totals from the EC method generally exceed corresponding totals from the aerodynamic method at both locations. The average difference in monthly total evaporation (computed as EC minus aerodynamic) at Padre Bay is 19.81 mm (0.78 in) or a bias of 23% relative to aerodynamic estimates. The average difference in monthly total evaporation between methods at Warm Creek Bay is 15.3 mm (0.6 in) or a bias of 17% relative to aerodynamic estimates. These differences represent the average difference computed across all months in the study period and indicate that monthly differences in evaporation totals between methods are larger than monthly differences in evaporation totals between sites.

Monthly evaporation totals from all possible methods are summarized in Figure 14 and Appendix 3. EC data are shown as bars, while all other methods are shown as lines. Results indicate that monthly totals from the EC method exceed monthly totals from the aerodynamic method at Padre Bay in all months except December 2021, which is a partial month. Similarly, monthly EC totals at Warm Creek Bay exceed corresponding monthly aerodynamic totals in all months except three (March 2019, June 2020, and November 2021). During 2019, monthly total evaporation peaks during September at both locations. During the other two years, monthly total evaporation peaks during August. This difference in timing of peak evaporation could be related to variations in water level experienced over the study period. Water levels were highest during the first year of observation (August 2019) and generally declined after (e.g., section 1.4). This finding demonstrates that the month of peak evaporation may change from one year to another.
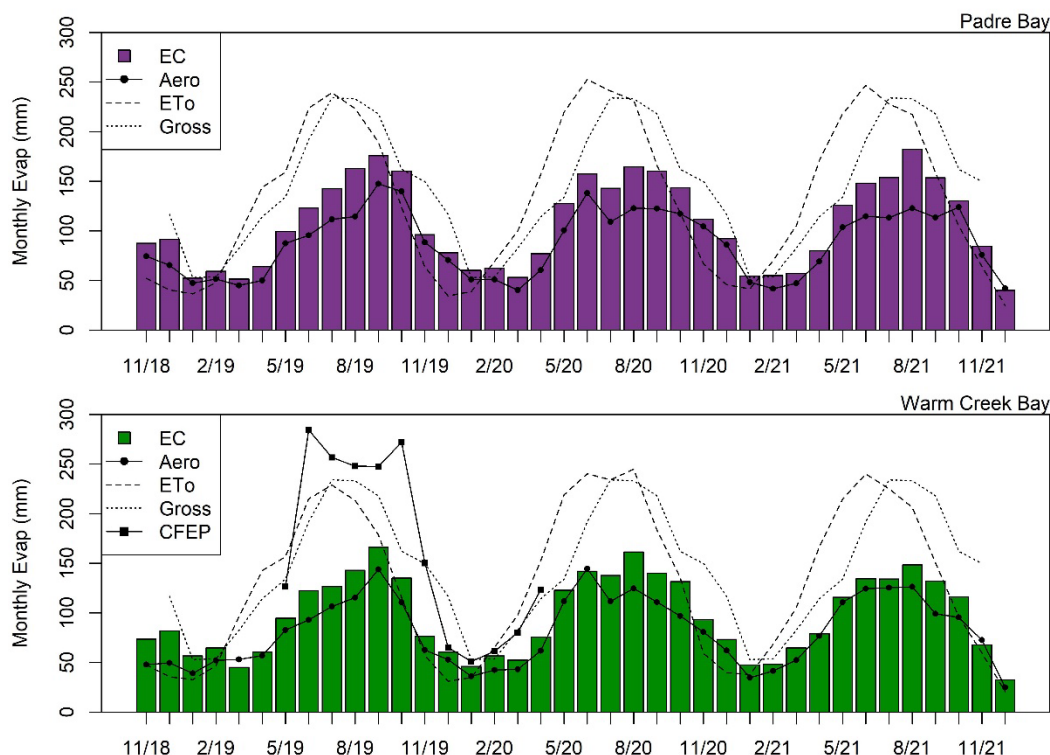
Figure 14—Monthly evaporation totals (mm) based on EC, aerodynamic, reference ET, gross evaporation coefficients, and CFEP valid at (top) Padre Bay and (bottom) Warm Creek Bay during the study period.

Additional results in Figure 14 show that monthly ETo peaks in June of each year at each location following Northern Hemisphere solar radiation. The gross evaporation coefficients are typically greater than monthly EC and aerodynamic totals; a few exceptions exist during winter months. We see that gross evaporation coefficients are similar to monthly ETo totals, a finding that demonstrates how Class A pan evaporation data (which informed the gross evaporation method) is closer to reference evapotranspiration than reservoir evaporation at this location. Monthly CFEP totals generally agree with the other estimates during winter months (e.g., December 2019, January 2020, and February 2020). However, during the warm season (May through November 2019), CFEP estimates greatly exceed EC, aerodynamic, and some ETo and gross evaporation coefficients. See Reclamation (2021) for additional details on the CFEP as applied at Lake Powell.

4.1.3 Yearly Time Scale

Differences in monthly evaporation totals integrate over time to produce differences in yearly evaporative losses. Totals for each (calendar) year of this study are listed in Table 4.1 and shown graphically in Figure 15. We exclude CFEP results because the period of record for that dataset is split between two calendar years. Results in Table 4.1 and Figure 15 agree with monthly results

30

discussed above, where EC evaporative totals exceed aerodynamic totals at both sites. Furthermore, three methods (EC, aerodynamic, and reference ET) show higher evaporative losses at Padre Bay compared to Warm Creek Bay. Results also show that evaporation totals during 2019 were lower than evaporation totals during 2020 for each method listed (except the gross evaporation coefficients, which do not vary).

Table 4.1—Annual evaporation totals (mm) as a function of calendar year. Values in parentheses are in units of feet. Years 2018 (November 7 through December 31) and 2021 (January 1 through December 16) represent partial totals.

Year	Padre Bay			Warm Creek Bay			Gross Evap
	EC	Aero	ETo	EC	Aero	ETo	
2018	179.01 (0.59)	139.85 (0.46)	92.61 (0.3)	155.51 (0.51)	97.65 (0.32)	83.23 (0.27)	-
2019	1265.25 (4.15)	1049.39 (3.44)	1579.99 (5.18)	1151.21 (3.78)	968.99 (3.18)	1515.02 (4.97)	1743.71 (5.72)
2020	1352.98 (4.44)	1103.96 (3.62)	1707.14 (5.60)	1232.97 (4.05)	1027.23 (3.37)	1707.31 (5.60)	1743.71 (5.72)
2021	1265.46 (4.15)	1016.76 (3.34)	1650.31 (5.41)	1120.59 (3.68)	984.51 (3.23)	1592.05 (5.34)	-
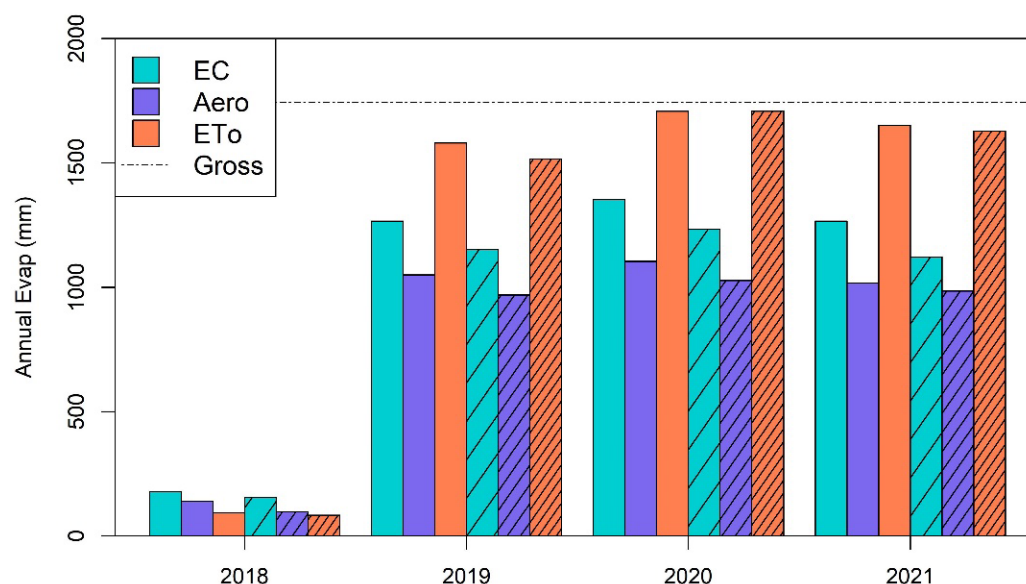
Figure 15—Yearly evaporation totals (mm) at Padre Bay (solid bars) and Warm Creek Bay (hatched bars) based on three methods during each calendar year of the study. Gross evaporation coefficients (horizontal dash dot line) do not vary by year. Years 2018 (November 7 through December 31) and 2021 (January 1 through December 16) represent partial totals.

4.1.4   Mass Transfer Coefficient Calibration

The aerodynamic method applied in this study relies on MOST for estimation of the bulk mass transfer coefficient, Ce. Historical applications with limited data or processing capability have utilized fixed coefficients based on reservoir size and other static factors (Fisher et al. 1979; Brutsaert 1982). The massive amount of data provided by modern in-situ measurements allows us to understand how Ce varies independently of reservoir size alone. To account for unique reservoir characteristics and atmospheric exchange properties, calibration of Ce using independent evaporation estimates such as EC or energy balance estimates is recommended (Brutsaert, 1982). Our results show that Ce is a function of atmospheric stability and windspeed (Figure 16), where stability is defined by the Monin-Obukhov length, z/L. Stable is defined as z/L > 0, unstable is defined as z/L < 0, and neutral is defined as z/L= 0. Neutral conditions (z/L=0) occur when the iterative MOST Ce estimation fails to converge on either unstable or stable solutions. Similar to previous findings, neutral coefficients approach stable and unstable values at windspeeds greater than 8 m/s (Tanny 2007; Verburg and Antenucci 2010).
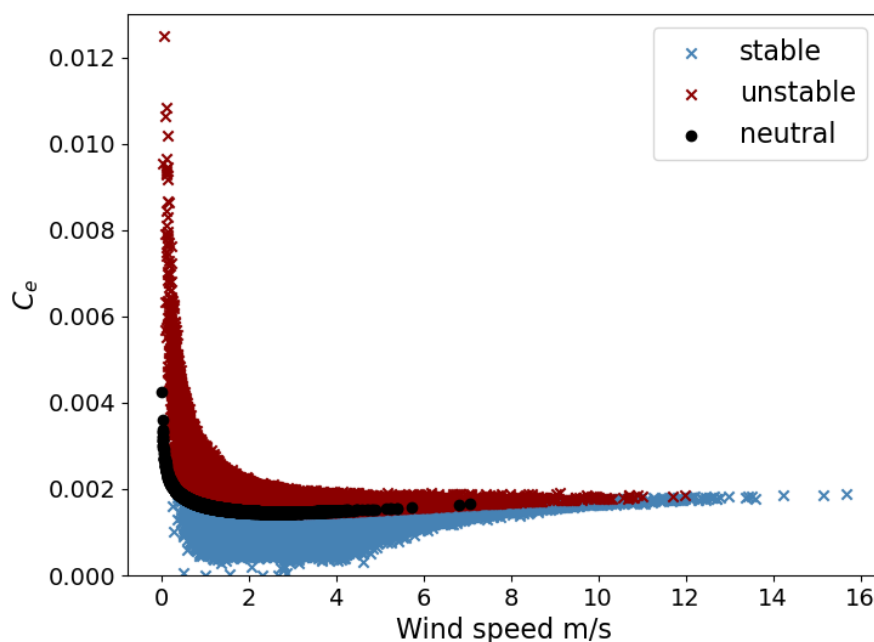
Figure 16—Scatterplot of MOST derived 30-minute mass transfer coefficient estimates, Ce, versus windspeed and stability at Padre Bay.

The scatterplot in Figure 16 demonstrates how the MOST transfer coefficient varies as a function of wind speed and atmospheric stability at the 30-minute time scale. The transfer coefficient also varies as a function of month. Figure 17 shows box and whisker plots of 30-minute Ce values plotted as a function of month and year at both locations. Notice the restricted data availability range, which is

associated with the loss of data during the beginning of the study period. Monthly median values of Ce generally peak during cool season months (e.g., October through March) at both locations, with median values reaching a minimum during warm season months (April through August). The lower Ce values experienced during warm season months is likely related to stable atmospheric conditions that develop over water bodies when water temperatures are cooler than air temperatures above (i.e., stably stratified). The opposite tends to be true during the cool season when water temperatures exceed overlying air temperatures. This behavior has been documented on other large lakes (e.g., Spence et al. 2011; Holman et al. 2012).
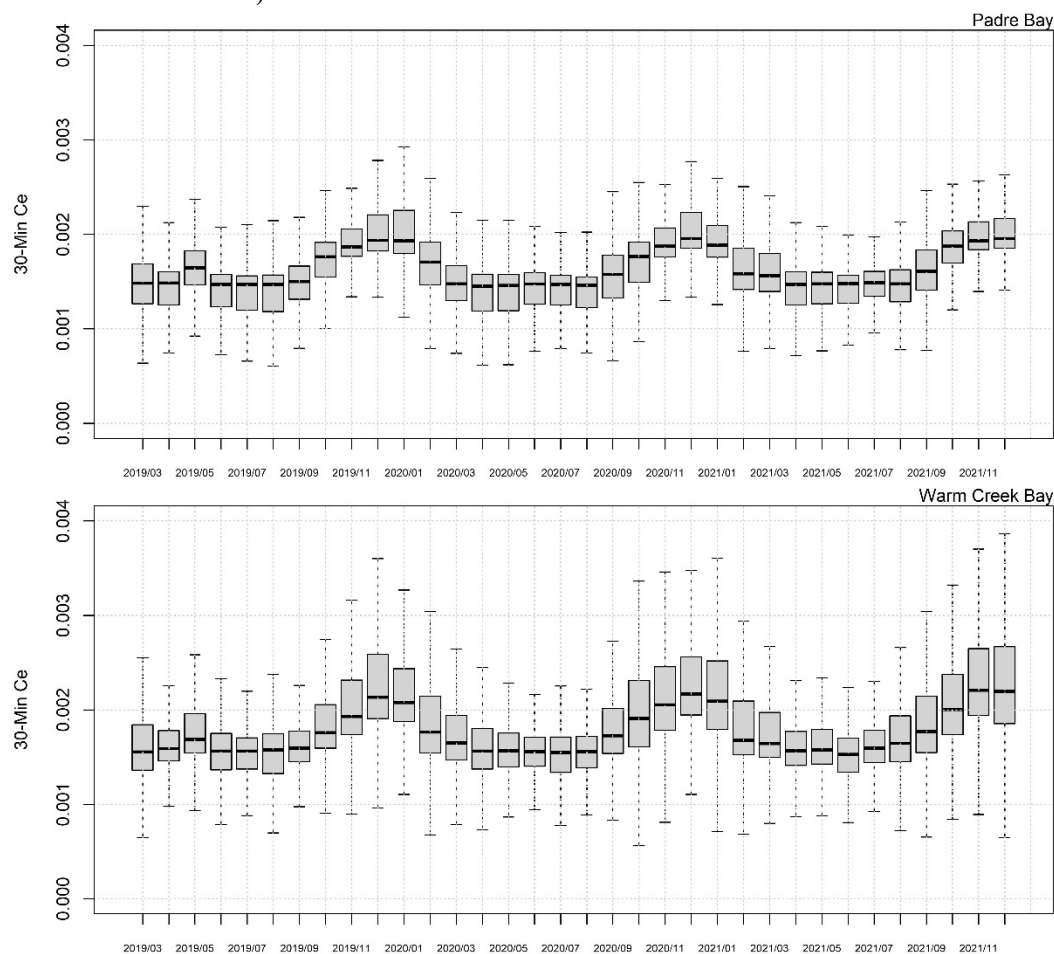
Figure 17—Box and whisker plots of 30-minute Ce values as a function of year/month at (left) Padre Bay and (right) Warm Creek Bay. Thick horizontal lines represent the population median. Shaded rectangles extend to the 25th and 75th percentiles. Whiskers extend to 1.5 times the inter-quartile range.

Relative to EC, the aerodynamic approach represents a more cost-effective option for long-term monitoring. However, results in Figure 14 and Figure 15 suggest that evaporation estimates from the aerodynamic method (as applied in this study) are underestimated relative to the EC method at monthly and yearly time scales. We propose two different methods for modifying the MOST bulk mass transfer coefficients to help remedy this finding. The first method involves estimating the bulk mass transfer coefficient by substituting daily EC evaporation and daily average wind speed, saturated specific humidity, and 2 m specific humidity into Equation 2 and solving for Ce. More specifically, Ce is estimated as the slope of a linear regression between the two variables (evaporation and the product of the latent heat of vaporization, wind speed, and saturated specific humidity of the water surface temperature minus the 2 m specific humidity) forced through the intercept. We apply this approach to 30-minute observations from Padre Bay and Warm Creek Bay and estimate a monthly average Ce value for each month separately (see supplemental plots in Appendix 2.3.2). We refer to this method as the EC-based approach. The second method involves calibrating the MOST-derived Ce estimates using results from the EC method as "truth". Specifically, we develop a Ce correction factor by taking the ratio of multi-year average monthly total EC evaporation (12 values) to multi-year average monthly total aerodynamic evaporation (12 values) and multiplying the resulting coefficient by the existing multi-year average monthly average Ce value. We refer to this approach as the scale-factor approach.

Monthly bulk mass transfer coefficients from the three different approaches (MOST-derived, EC-based, and scale factor) are shown in Figure 18. Results indicate that at Padre Bay, the EC-based and scale-factor based Ce estimates exceed the MOST estimates during each month. At Warm Creek Bay, this finding does not hold true. Instead, the EC-based Ce values are less than the MOST-based values between April and August. During the remainder of the year, the EC-based Ce values exceed the MOST-based values. As with Padre Bay, the scale-factor based Ce values exceed the MOST-based values during every month at Warm Creek Bay. We do not use these coefficients in the current study. Rather, we present these adjustments to demonstrate how aerodynamic evaporation estimates could be modified at this location in the absence of EC data.
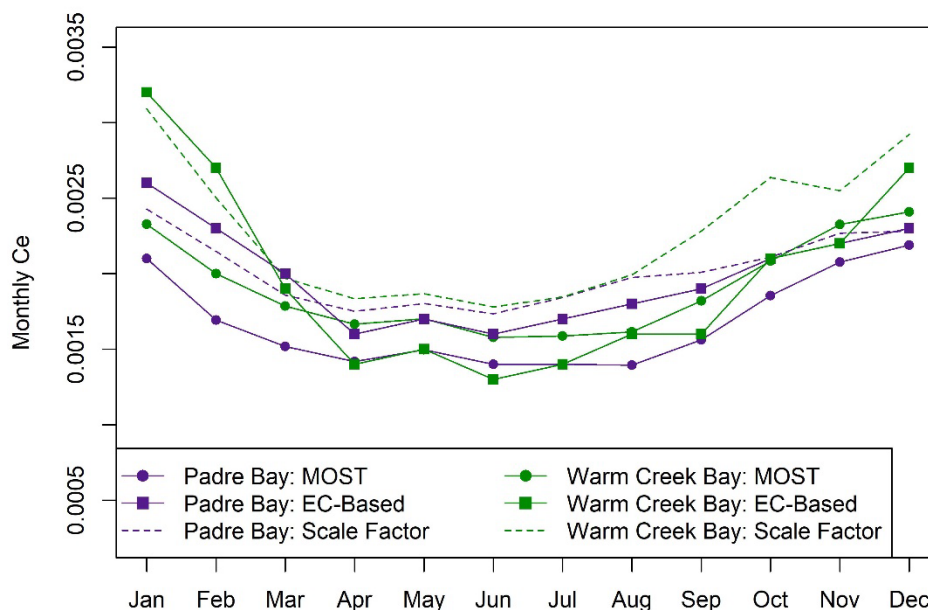
Figure 18—Average monthly Ce values computed over all years at Padre Bay and Warm Creek Bay based on the original MOST method, EC-based approach, and scale-factor approach.

Direct comparison of transfer coefficients from other studies and lakes is difficult due to the dynamic nature and dependence of Ce on windspeed, measurement heights, and atmospheric stability. Ce estimates from this study fall within the range of other mass-transfer values reported in the literature. For example, Harbeck (1962) utilized a constant transfer coefficient of 0.0019 for Lake Hefner, a reservoir located in Oklahoma (note that Harbeck Ce values were converted to SI units and reported by Tanny, 2008). Tanny (2008) estimated constant Ce values of 0.00194 and 0.00188 for unstable conditions at measurement heights of 0-0.9 m and 0-2.9 m, respectively, for a small reservoir in Israel. Finally, Verburg and Antenucci (2010) highlighted the importance of stability adjustments when estimating Ce and reported an average Ce value of 0.00185 for a one-year study at Lake Tanganyika.

4.2 Gridded Climate and Remote Sensing Comparisons

Continuous data collection that captures the spatial and temporal variability of over-water conditions is difficult and costly to maintain. Therefore, long-term, operational estimation and evaluation of reservoir evaporation likely requires the use of remotely sensed and/or gridded climate datasets to capture such variability. A secondary objective of the current project is to utilize over-water observations to assess the representativeness of readily available gridded climate and remote

sensing datasets at Lake Powell and assess their potential for application within reservoir evaporation models for long-term modeling and prediction.

4.2.1 Gridded Weather Comparison

Many gridded climate products do not acknowledge or account for the presence of large water bodies in their land surface modeling. Furthermore, when present, many water mask adjustments fail to provide accurate estimates of over-water weather. Evaporative cooling affects the condition of the atmosphere above a water body, leading to cooler temperatures and increased humidity. Not accounting for the presence of water in near-surface modeling overestimates air temperature and the vapor pressure deficit (VPD), which in turn leads to overestimates of evaporation when applying traditional approaches that rely on accurate weather forcing information such as aerodynamic methods.

For this work, we focus on the Real-time Mesoscale Analysis (RTMA) climate dataset (De Pondeca, 2011). RTMA provides hourly estimates of near-surface weather conditions including air temperature, specific humidity, atmospheric pressure, and wind speed at 2.5-km resolution. Importantly, RTMA incorporates buoy-based datasets and utilizes a land/water mask to restrict the interpolation of land-based observations over water (De Pondeca, 2011). Incoming solar radiation estimates were derived from the North American Land Data Assimilation System-2 (NLDAS-2, Xia, Youlong, et al, 2012) to fulfill all forcing requirements of many open-water evaporation models as well as reference ET. Previous work focusing on agricultural areas demonstrates that RTMA can capture evaporative cooling effects related to irrigation applications not directly accounted for in other forcing datasets such as gridMET (Blankenau, 2020).

Intercomparisons of daily RTMA and NLDAS observations with in-situ observations at the two reservoir sites from November 2018- December 2021 are shown in Figure 19. RTMA data represents a spatial average of all water masked grid cells intersecting Lake Powell. The NLDAS solar radiation observations generally underestimated solar radiation relative to in-situ observations, with bias estimates (indicated by the slope through zero) of 0.94 for both locations, RMSE values between 10.996 and 11.560 W/m^2, and R^2 values of 0.98 (bottom plot of Figure 19). R^2 values close to 1 indicate good correlation and ability to simulate temporal variability. RMSE values of RTMA and in-situ air temperature at Padre Bay and Warm Creek from 2019-2021 were 0.93 and 0.85 degrees C, respectively. Daily average wind speed estimates from RTMA were consistently lower than in-situ station measurements. Slope values for Padre Bay and Warm Creek were 0.80 and 0.91, respectively. The lower wind speeds in RTMA may be an artifact of its use of surface aerodynamic roughness characteristic of vegetation and surrounding terrain during data generation rather than the smoother roughness for open water. The open water roughness produces a steeper wind profile above water and higher wind speeds near the water surface. RTMA VPD estimates show

36

a relatively high bias relative to in-situ station measurements (slope values of 1.11 and 1.09 for Padre Bay and Warm Creek, respectively). Observed VPD bias is a product of biases in both air temperature and specific humidity where increased temperatures lead to increased VPD when the amount of water vapor in the air remains constant.
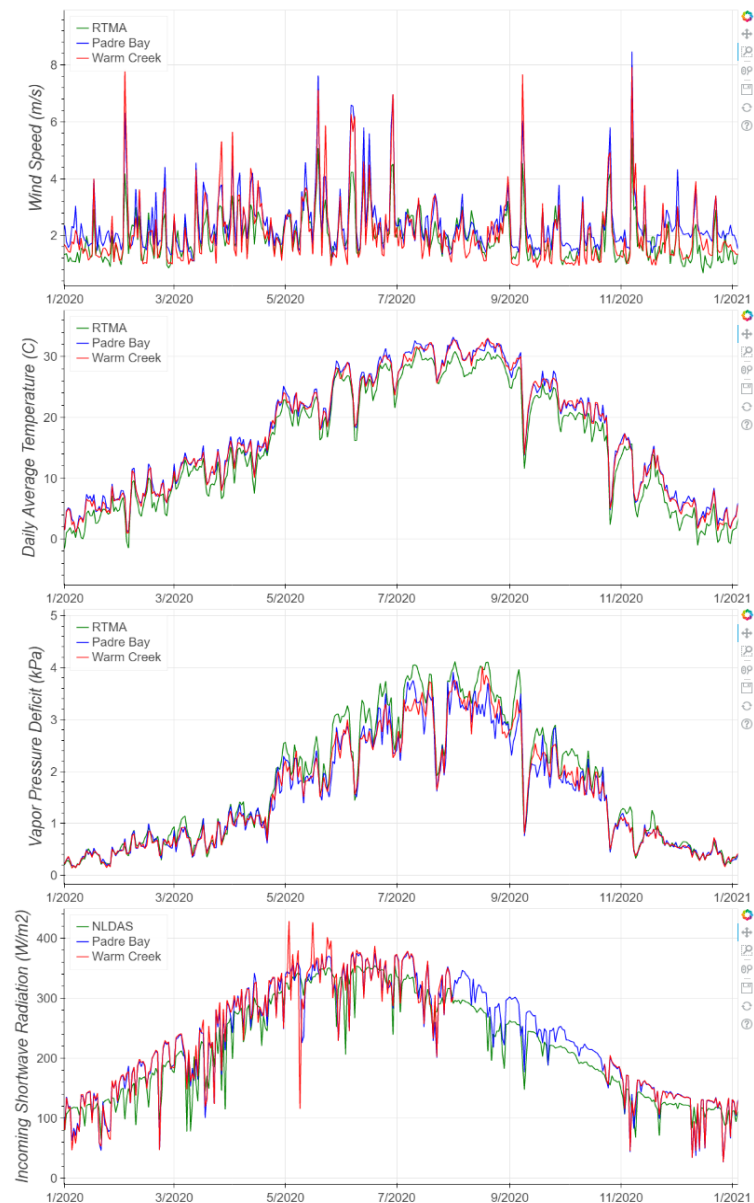
Figure 19—Timeseries plot of reservoir average RTMA estimates with in-situ observations of wind speed, air temperature, vapor pressure deficit, and incoming shortwave from Padre Bay and Warm Creek stations during 2020.

Many models of reservoir evaporation, such as the Complementary Relationship Lake Evaporation Model (Morton, 1983) and the Texas A&M Lake Evaporation Model (Zhao and Gao, 2019), employ internal conditioning functions to adjust land-based weather datasets to represent over-water settings. However, the accuracy of these conditioning functions can vary widely depending on location and environment. Results from this comparison demonstrate the ability of RTMA to capture seasonal patterns in over-water weather conditions. Evaporative cooling effects, not accounted for in other gridded climate products, are somewhat represented within RTMA, however, further refinement and testing is needed prior to direct (i.e., out-of-the-box) application of RTMA at all locations and reservoirs. Results from this comparison demonstrate the ability of RTMA to accurately estimate over-water settings, opening opportunities for improved reservoir evaporation modeling.

4.2.2 Landsat Surface Temperature

The Landsat Program provides high resolution (~100-m resolution) land surface temperature (LST) observations at 8-to-16-day satellite overpass frequency since 1985. Unless explicitly stated, we use LST to refer to both land and water surface observations. Landsat LST is an instantaneous snapshot collected at approximately 11:00 AM each overpass day. Other satellite platforms provide more frequent image collection; however, they often sacrifice spatial resolution for improved temporal coverage (e.g., MODIS daily LST observations at 1000-m resolution). Use of Landsat helps to avoid interference of land and shallow regions. To avoid issues with Landsat 7 orbital drift and image acquisition time variability, we focus only on Landsat 8 comparisons for this analysis. It should be noted that the Landsat 8 thermal infrared sensor collects data at 100-m resolution and values are resampled to 30-m resolution during processing. Figure 20 shows January, April, July, and October monthly averages of Landsat 8 LST observations from 2014 to 2021 for the southwest region of Lake Powell. Spatial variability in LST changes dynamically throughout the year depending on reservoir characteristics, such as fetch and depth. Note how surface temperatures at Padre Bay (central portion of the figure) remain higher than other areas during the winter months due to greater depth and increased heat storage.
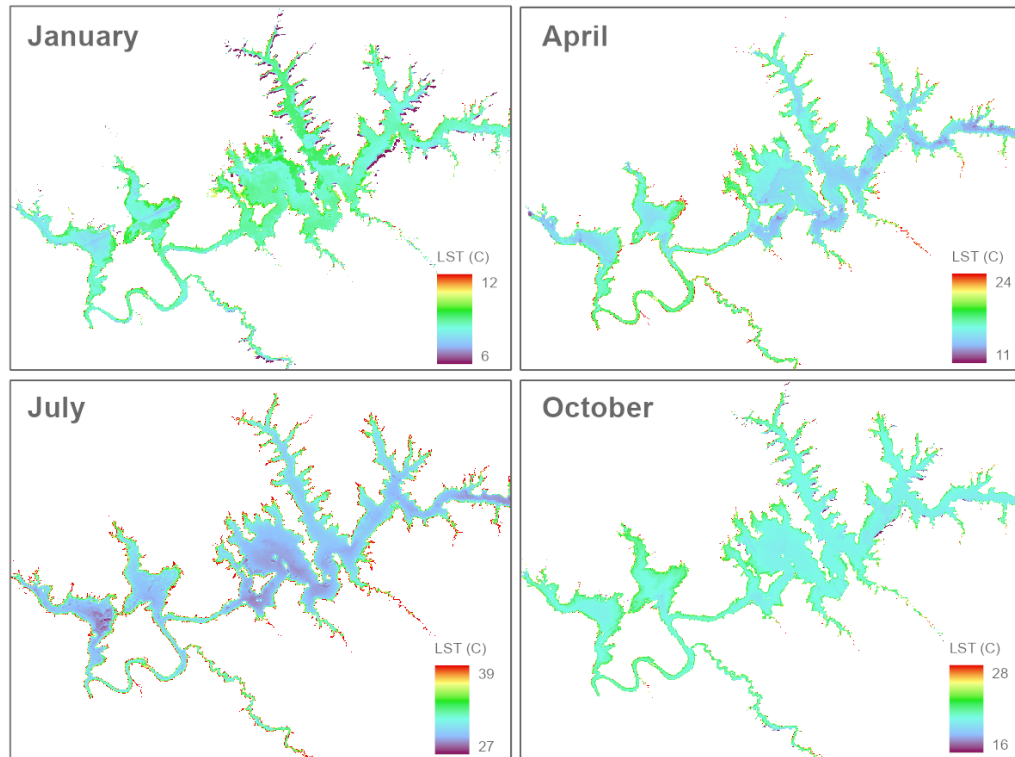
Figure 20—Monthly average Landsat 8 Land Surface Temperature from 2014-2021 for January, April, August, and October.

Landsat 8 LST from each monitoring station's coincident Landsat pixel correlated well with in-situ IRT-based skin temperature data at both Padre Bay and Warm Creek study sites (R^2 of 0.959 and 0.944, respectively; Figure 21). Both sites had positive bias between in-situ skin temperature and satellite LST observations (slope through zero of 1.071 and 1.070 and mean bias of 1.24 and 1.27 °C for Padre Bay and Warm Creek, respectively). Expansion of the Landsat LST footprint to include additional pixels surrounding the monitoring platforms show similar statistical relationships to the coincident pixel comparisons (data not shown).

There are numerous reasons why satellite LST estimates are not in perfect agreement with in-situ observations. Skin temperature collected at each monitoring platform is based on 30-minute average conditions between 11:00 AM and 11:30 AM which is slightly out of synchronization with Landsat's instantaneous observation (~11:02 AM). Other reasons for differences in temperature may include spatial resolution (i.e., 30-m vs point measurement), inclusion of the monitoring platform within the Landsat pixel (i.e., dock surface relative to water surface), satellite cloud masking, atmospheric corrections, and in-situ correction assumptions such as the emissivity of water, as well as incoming long-wave correction of the IRT measurements. IRT data collected

during this study is not ideal for LST validation due to platform motion and the frequent influence of artifacts such as spider webs and dust (refer to section 1.3.1.1 and Reclamation, 2021). However, strong correlations between in-situ observations collected and satellite-based estimates improve confidence for future modeling applications and use of remote sensing datasets for continuous, broad-scale estimation of reservoir evaporation. Additional investigation is needed to understand spatial variability in lake surface temperatures and the potential influence of the positive bias on remotely sensed evaporation estimates.
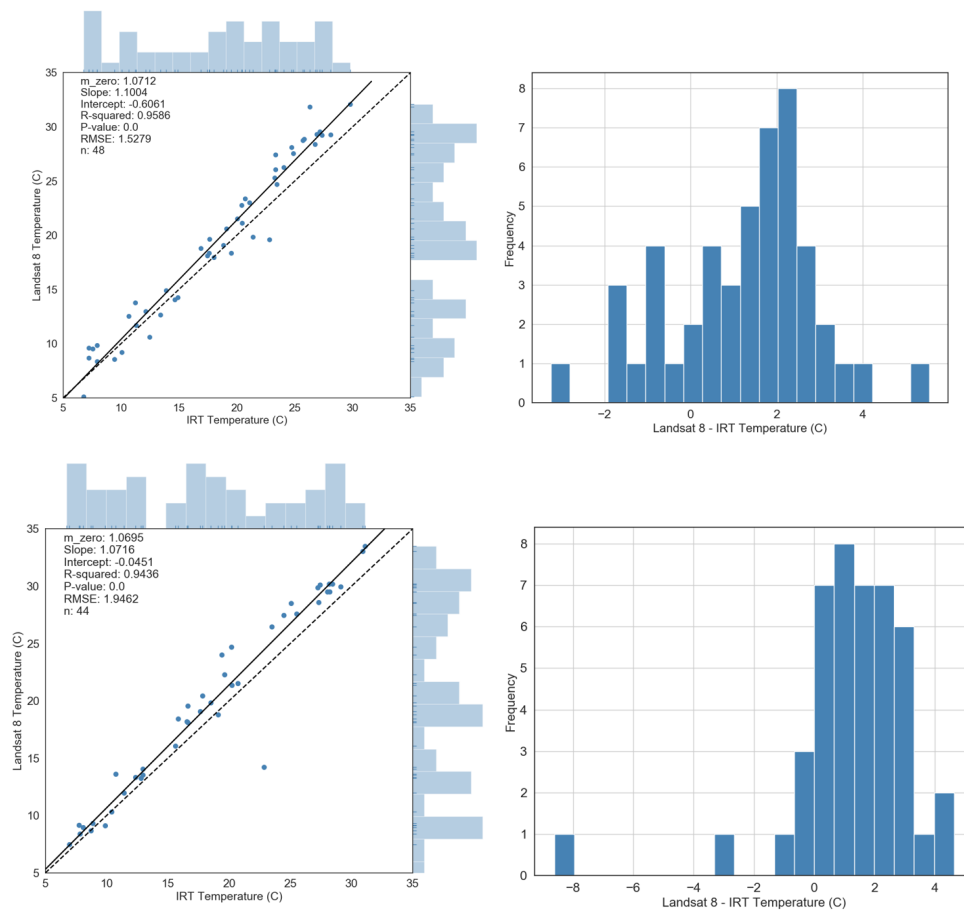
Figure 21—Scatterplot and distribution of differences comparing average skin temperature observations valid between 11:00 AM to 11:30 AM MST with Landsat 8 LST observations from the coincident 30-m pixel at (top) Padre Bay and (bottom) Warm Creek Bay locations. Least square linear regression line is shown as solid black, while the y=x line is shown as dashed black. Distribution of temperature values is shown using bar plots along each respective axis. Differences are calculated as Landsat 8 temperature minus IRT temperature.

4.2.3   Remotely Sensed Reservoir Evaporation

Remote sensing models (RSMs) utilize satellite-based visible and infrared surface measurements combined with meteorological data to estimate individual components of the surface energy balance or to scale reference evaporative demand values to actual conditions. Multiple RSMs capable of estimating reservoir evaporation exist in the literature (Abdelrady 2016; Allen 2007; Zhao 2021), however, few if any, have been used in operational settings. Lack of consistent, high quality in-situ datasets leads to limited validation, creating uncertainty when applying these methods to new regions and systems. Furthermore, large differences in evaporation estimates from in-situ methodologies create further uncertainty during accuracy assessment (Metzeger 2018; Mosner 2003; Westerhoff 2015).

The Lake Powell monitoring stations provide benchmark evaporation estimates based on over-water measurements using best available science and techniques. These estimates are representative of two large bays at Lake Powell, but differences in water temperature and near-surface weather conditions throughout the reservoir lead to spatially varying evaporation rates. It is likely that using a combination approach based on gridded climate data and remotely sensed surface temperature can help to capture these variations and improve estimates of total reservoir evaporation. Furthermore, in addition to capturing spatial variability, the incorporation of water temperature data helps to account for the impact of heat storage as well as inflow and outflow dynamics.

Most RSMs utilize evaporation estimates at the time of satellite overpass along with hourly and daily climate relationships to scale from instantaneous estimates to daily values. Daily evaporative fraction values derived on satellite overpass days are then interpolated and combined with daily meteorological forcing data to compute longer-term evaporation time series. Uncertainty in climate forcing data and the variability of instantaneous observations relative to longer-term values can be problematic during scaling to daily and monthly estimates. For example, evaporation is highly sensitive to wind speed which can be extremely variable at short time scales. Additionally, the use of land-based gridded climate datasets for over-water applications can lead to overestimation, especially in arid and semi-arid regions where over-water conditions are drastically different from the surrounding landscape.

As proof of concept, we present preliminary evaporation estimates from OpenET's application of AquaSEBS (Abdelrady, 2016) within the PTJPL (Priestly-Taylor Jet Propulsion Laboratory) model (Fisher, 2018). AquaSEBS utilizes an Equilibrium Temperature Model based on surface temperature, albedo, wind speed, humidity, and solar radiation to estimate evaporation at the time of the satellite overpass. The instantaneous estimate is then upscaled to daily through a fractional scaling approach based on instantaneous and daily net radiation.

Currently, OpenET's PTJPL implementation relies on Landsat for surface temperature and albedo and NLDAS-2 for air temperature, vapor pressure, and incoming shortwave and longwave radiation. PTJPL evaporation estimates are produced for each 30-m Landsat pixel throughout the water body.

For this comparison, spatially weighted PTJPL evaporation estimates were extracted for each monitoring site for all cloud-free satellite overpass days using dynamic footprints based on the EC analysis. Comparison of daily estimates taken on satellite overpass days with daily EC estimates (Figure 22) shows bias values of 1.02 and 1.17 (i.e., biases of 2% and 17%) and RMSE of 2.2 and 2.7 mm for Padre Bay and Warm Creek, respectively. R^2 values for Padre Bay and Warm Creek were 0.28 and 0.20, with the low R^2 driven primarily by a clear mismatch in seasonal evaporation timing (i.e., premature peak). Landsat LST comparisons show good correlation and a high bias relative to in-situ observations (see section 4.6.2). Disagreements between PTJPL and in-situ EC estimates are potentially driven by uncertainty and bias in the meteorological forcing dataset and simulated energy balance. NLDAS-2 is a 12-km resolution product that does not actively adjust for over-water conditions or account for the surrounding arid landscape and complex terrain. In addition, NLDAS wind speed estimates are derived from large-scale (32-km) North American Regional Reanalysis (NARR) model simulations that do not capture the synoptic daily variability in winds well. Future RSM applications with high-resolution climate datasets, such as RTMA, and incorporation of over-water adjustments and/or bias corrections based on in-situ measurements will help improve forcing data and in turn help RSMs better simulate reservoir evaporation.
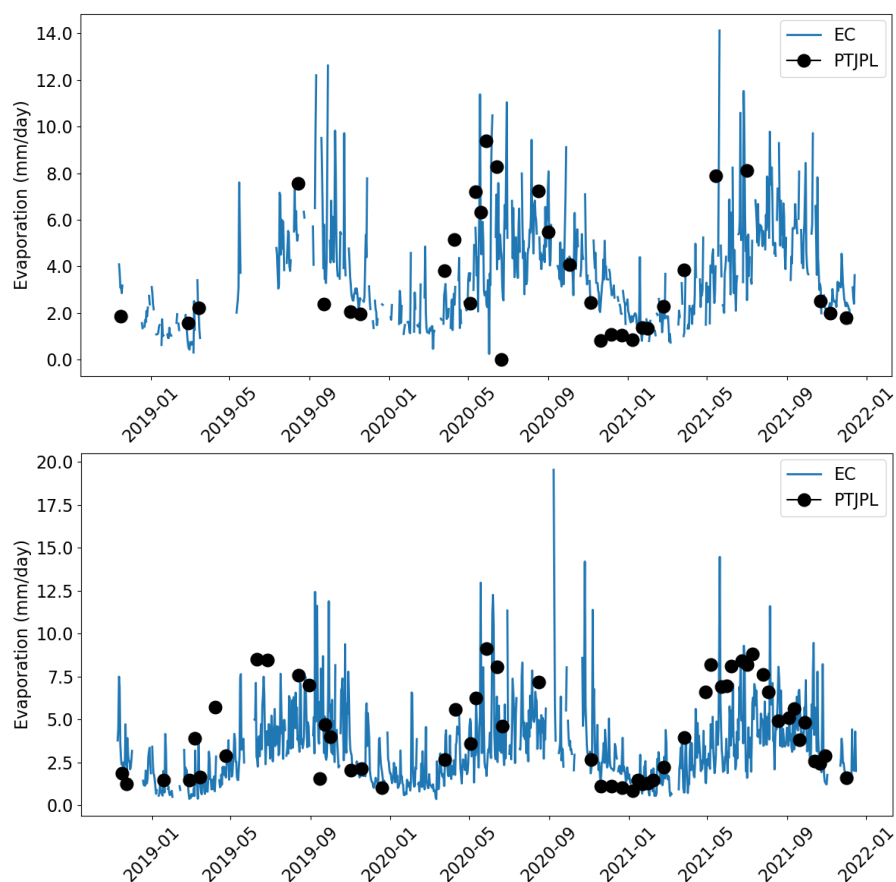
Figure 22—Time series plot of daily EC evaporation estimates (non-gap filled), and remotely sensed evaporation estimates from the PTJPL RSM on satellite overpass days at (top) Padre Bay and (bottom) Warm Creek Bay.

Open ET's PTJPL demonstrates one method of estimating reservoir evaporation using satellite data. Other RSM approaches exist that utilize different satellite platforms and are less reliant on the scaling of instantaneous estimates. For example, Texas A&M University recently developed a Lake Evaporation Model (LEM) that utilizes fetch-based conditioning functions to account for evaporative cooling effects and an internal heat storage simulation to estimate heat storage (Zhao, 2019). Model developers are working to couple LEM with remotely sensed surface temperature from MODIS (moderate resolution imaging spectroradiometer) for improved tracking and simulation of water temperature (Zhao, 2021). While MODIS offers more frequent overpass timing, the reduced spatial resolution of 1000 m is not adequate for LST measurement at all reservoirs. Further testing, intercomparisons, and validation work is needed to identify strengths and weaknesses of each approach as well as the impact of different satellite and climate forcing datasets.

5 Discussion

Although we utilized state-of-the-art instrumentation and data processing methods to produce evaporation estimates at Padre Bay and Warm Creek Bay, limitations exist. For example, all datasets were impacted (to various degrees) by data gaps. We implemented a gap-filling procedure that has been documented in the literature and applied to EC data. However, alternative gap filling methods exist and could result in different estimates.

Secondly, the EC evaporation estimates presented in this study have not been corrected for energy budget closure imbalances. Energy budget imbalances occur when the sum of the turbulent fluxes does not equal the sum of net radiation and change in heat storage. The heat storage term is notoriously hard to quantify, and there is some debate within the scientific community whether or not the correction is needed (e.g., Foken et al., 2012). While Moreo and Swancar (2013) and Earp and Moreo (2021) account for the energy imbalance issue in evaporation computations at Lake Mead and Lake Mohave, the task is less practical at Lake Powell due to the lack of data on some of the energy sources and sinks to the system. Consequently, we acknowledge this limitation here.

The third limitation of this study relates to the aerodynamic method. More specifically, comparisons between EC estimates and aerodynamic estimates as implemented in this work suggest that the bulk mass transfer coefficient based on MOST may be under-estimated during certain times of year. Estimating the bulk mass transfer coefficient using EC evaporation estimates as truth is an alternative way for estimating the coefficient. Similarly, adjusting the MOST-based mass transfer coefficient so that monthly aerodynamic totals equal monthly EC totals is a second (less common) way to address this difference. Although we presented two methods for updating the bulk mass transfer coefficients, we do not propose to use them unless EC data are missing.

Finally, the evaporation estimates presented in this report are representative of two of Lake Powell's larger bays. Complex bathymetry, wind, and temperature dynamics lead to varying evaporation rates across the reservoir surface. Previous measurements and studies performed in other regions of the reservoir or at locations closer to shore with limited fetch may be biased high relative to stations located at the center of the water body.

In the future, updated evaporation estimates produced in this study will be shared with the Power Office of the Upper Colorado Basin Regional Office for evaluation in their hydrologic modeling system. As data collection continues, reservoir evaporation estimates from the current study (i.e., three years of EC and aerodynamic results) will also be used to support other ongoing operational

evaporation studies at Reclamation. Specifically, the Padre Bay and Warm Creek Bay evaporation time series may be used for validation and comparison of alternative remote sensing datasets, including a dataset generated using the Lake Evaporation Model (LEM) developed by Zhao and Gao (2019).

6 Summary

Lake Powell is the second largest man-made reservoir by water capacity in the United States, second only to Lake Mead. Estimates of evaporative losses from Lake Powell are used to support hydrologic modeling and decision making in the Upper Colorado River Basin. Present-day estimates of monthly evaporation rates from Lake Powell, referred to as gross evaporation coefficients, are based on historical estimates developed by Reclamation (1986) and are static and do not reflect variable climate conditions. To support improved water resource management in the Upper Colorado River Basin, Reclamation partnered with the Desert Research Institute (DRI) to develop alternative estimates of evaporation from Lake Powell using modern in-situ methods.

In this study, we developed sub-daily, daily, monthly, and yearly evaporation totals from Lake Powell using two independent methods valid between November 7, 2018, and December 16, 2021. These methods, which include eddy covariance (EC) and bulk aerodynamic, were based on over-water observations recorded via floating platforms at two different locations on Lake Powell. The EC method is often considered the gold standard for evaporation estimation within the scientific community (e.g., Moreo 2013), although the aerodynamic approach is often easier to implement, experiences fewer instrumentation outages, and is less expensive overall (e.g., Friedrich et al. 2018).

Results from the current study indicate that EC and aerodynamic estimates agree well at daily and monthly time scales, with weaker agreement between the two datasets at the 30-minute time scale (at both locations). There is a slight negative bias in daily and monthly aerodynamic estimates relative to EC estimates, which can be addressed by adjusting the bulk mass transfer coefficient. Beyond in-situ methods, we compared monthly, and annual totals developed in the current study with alternative datasets available for Lake Powell (gross evaporation coefficients, reference ET, and CFEP). Results showed that monthly evaporation totals from the three additional datasets generally exceeded corresponding totals from both the EC and aerodynamic methods.

Long-term operation of over-water instrumentation is expensive and difficult. Therefore, we explored how observations obtained in the current study compared with remotely sensed and gridded weather datasets to support alternative methods of estimating reservoir evaporation. Comparison of over-water observations with

gridded estimates from RTMA show good correlation; however, additional corrections are needed to fully capture evaporative cooling effects on modeled air temperature and relative humidity and over-water surface roughness impacts on modeled wind speed. Preliminary assessment of remotely sensed evaporation estimates from the PTJPL AquaSEBs model on satellite overpass days shows large seasonal biases based on estimates driven using forcing data from NLDAS-2. Application of AquaSEBs with high-accuracy forcing data (e.g., RTMA) will likely improve evaporation estimates and model skill.

7 Acknowledgements

8 References

Abdelrady, Ahmed, et al. "Surface energy balance of fresh and saline waters: AquaSEBS." *Remote sensing* 8.7 (2016): 583.

Alavi, N, J.S. Warland, and A.A. Berg, 2005. Filling gaps in evapotranspiration measurements for water budget studies: Evaluation of a Kalman filtering approach. *Agricultural and Forest Meteorology*, **141**, 57-66.

Allen, Richard G. "Standard Reference Evapotranspiration Calculations: REF-ET." *Irrigation and Drainage: Saving a Threatened Resource—In Search of Solutions*. ASCE, 1992.

Allen, Richard G., et al. "Satellite-based energy balance for mapping evapotranspiration with internalized calibration (METRIC)—Applications." *Journal of irrigation and drainage engineering* 133.4 (2007): 395-406.

Andrews, B. D., Baldwin, W. E., Worley, C. R., Baskin, R. L., Denny, J. F., Foster, D. S., Irwin, B. J., Moore, E. M., & Nichols, A. R., 2018. High-resolution geophysical data collected in Lake Powell, Utah-Arizona, U.S. Geological Survey Field Activity 2017-049-FA [Data set]. U.S. Geological Survey. https://doi.org/10.5066/P90BU2VS

Apogee Instruments, 2015. Emissivity Correction for Infrared Radiometer Sensors. Available online: http://www.apogeeinstruments.com/emissivity-correction-for-infrared-radiometer-sensors/ (Accessed 2 July 2015).

ASCE-EWRI. 2005. The ASCE Standardized Reference Evapotranspiration Equation, Report 0-7844-0805-X, ASCE Task Committee on Standardization of Reference Evapotranspiration, Reston, Virginia., American Soc. Civil Engineers. Available at http://www.kimberly.uidaho.edu/water/asceewri/

Asquith, W.H. and J.S. Famiglietti, 2000. Precipitation areal-reduction factor estimation using, and annual-maxima centered approach. Journal of Hydrology, **230**(1), 55-69.

Aubinet, M., T. Vesala, D. Papale, 2012. Eddy Covariance A practical guide to measurement and data analysis. Springer. 447 pp.

Baldocchi, D. D., Hincks, B. B., & Meyers, T. P. (1988). Measuring biosphere-atmosphere exchanges of biologically related gases with micrometeorological methods. Ecology, 69(5), 1331–1340. https://doi.org/10.2307/1941631

Blankenau, P.A., Kilic, A. and Allen, R., 2020. An evaluation of gridded weather datasets for the purpose of estimating reference evapotranspiration in the United States. *Agricultural Water Management*, 242, p.106376.

Brutsaert, W. (1982), Evaporation into the Atmosphere: Theory, History, and Applications, 299 pp., Kluwer Academic Publishers, Dordrecht, The Netherlands.

Brutsaert, W. (2005), Hydrology: An Introduction, 605 pp., Cambridge Univ. Press, New York.

Campbell Scientific, EasyFlux PC Eddy Covariance Post Processing PC Software, 2017.

Campbell Scientific, 2022. EASYFLUX DL CR6OP or CR1KXOP For CR6 or CR1000X and Open-Path Eddy-Covariance Systems. 185 pp.

Clayton, R. "Upper Colorado River Consumptive Use Determination at CRSS Natural Flow Node 480 Locations Calendar Years 1971-1995, Methodology Peer Review." U.S. Bureau of Reclamation, Upper Colorado Region, Salt Lake City. (2004).

Clayton, R. "Reclamation Evaporation Methodology for Lake Powell." Unpublished Report. U.S. 478 Bureau of Reclamation, Upper Colorado Region, Salt Lake City, UT. (2008): 479.

Collison, J. (2019), The Collison Floating Evaporation Pan: Design, Validation, and Comparison. Dissertation submitted to the Civil, Construction, and Environmental Engineering Department at the University of New Mexico. 123 pp.

De Pondeca, Manuel SFV, et al. "The real-time mesoscale analysis at NOAA's National Centers for Environmental Prediction: current status and development." *Weather and Forecasting* 26.5 (2011): 593-612.

Earp, K.J., and Moreo, M.T., 2021, Evaporation from Lake Mead and Lake Mohave, Nevada and Arizona, 2010–2019: U.S. Geological Survey Open-File Report 2021–1022, 36 p., https://doi.org/ 10.3133/ ofr20211022.

Fisher, H. B., E. J. List, R. C. Y. Koh, J. Imberger, and N. H. Brooks (1979), Mixing in Inland and Coastal Waters, Academic, San Diego, Calif.

Fisher, J. (2018) Level-3 Evapotranspiration L3(ET_PT-JPL) Algorithm Theoretical Basis Document.

Foken, T. and Wichura, B. (1996) Tools for Quality Assessment of Surface-Based Flux Measurements. Agricultural and Forest Meteorology, 78, 83-105. https://doi.org/10.1016/0168-1923(95)02248-1

Foken, T., R. Leuning, S.R. Oncley, M. Mauder, and M. Aubinet, (2012). Corrections and Data Quality Control. Chapter 4.

Friedrich, K., Grossman, R. L., Huntington, J., Blanken, P. D., Lenters, J., Holman, K. D., Gochis, D., Livneh, B., Prairie, J., Skeie, E., Healey, N. C., Dahm, K., Pearson, C., Finnessey, T., Hook, S. J., & Kowalski, T. (2018). Reservoir Evaporation in the Western United States: Current Science, Challenges, and Future Needs, Bulletin of the American Meteorological Society, 99(1), 167-187. Retrieved Mar 23, 2022, from https://journals.ametsoc.org/view/journals/bams/99/1/bams-d-15-00224.1.xml

Harbeck, Guy Earl. *A practical field technique for measuring reservoir evaporation utilizing mass-transfer theory*. US Government Printing Office, 1962.

Heitjan, D. F., & Roderick J. A. Little. (1991). Multiple Imputation for the Fatal Accident Reporting System. *Journal of the Royal Statistical Society. Series C (Applied Statistics)*, *40*(1), 13–29. https://doi.org/10.2307/2347902

Holman, K. D., Gronewold, A., Notaro, M., and Zarrin, A. (2012), Improving historical precipitation estimates over the Lake Superior basin, Geophys. Res. Lett., 39, L03405, doi:10.1029/2011GL050468.

Hui, D., S. Wan, B. Su, G. Katul, R. Monson, Y. Luo, (2004), Gap-filling missing data in eddy covariance measurements using multiple imputation (MI) for annual estimations, Agricultural and Forest Meteorology, 121(1–2), https://doi.org/10.1016/S0168-1923(03)00158-8.

Huntington, Justin L., and Daniel McEvoy. *Climatological estimates of open water evaporation from selected Truckee and Carson River basin water bodies, California and Nevada*. Desert Research Institute, 2011.

Huntington, J.L., Gangopadhyay, S., Spears, M., Allen, R., King, D., Morton, C., Harrison, A., McEvoy, D., and A. Joros. (2015). West-Wide Climate Risk Assessments: Irrigation Demand and Reservoir Evaporation Projections. U.S. Bureau of Reclamation, Technical memorandum No. 68-68210-2014-01, 196 p., 841 app.

Huntington, Justin L., et al. "Climate Engine: Cloud Computing and Visualization of Climate and Remote Sensing Data for Advanced Natural Resource Monitoring and Process Understanding." *Bulletin of the American Meteorological Society* 2017 (2017).

Kljun, N., Kastner-Klein, P., Fedorovich, E., and Rotach, M. W., (2004). Evaluation of Lagrangian Footprint Model Using Data from a Wind Tunnel Convective Boundary Layer, Agr. Forest Meteorol., 127, 189–201

Kljun, N., Calanca, P., Rotach, M. W., and Schmid, H. P.: A simple two-dimensional parameterisation for Flux Footprint Prediction (FFP), Geosci. Model Dev., 8, 3695–3713, https://doi.org/10.5194/gmd-8-3695-2015, 2015.

Kohler, M.A., Nordenson, T.J., and Baker, D.R. (1959). Evaporation Maps for the United States. U.S. Dept. of Commerce, Weather Bureau, Technical Paper #37.

Kondo, J. 1975. Air-Seas Bulk Transfer Coefficients in Diabatic Conditions. Boundary-Layer Meterology 9:91-112.

La Rue, Eugene Clyde, and Hubert Work. *Water power and flood control of Colorado River below Green River, Utah*. No. 556. Govt. Print. Off.,, 1925.

Little, R.J.A., (1988) Missing-Data Adjustments in Large Surveys, Journal of Business & Economic Statistics, 6:3, 287-296, DOI: 10.1080/07350015.1988.10509663

Massman, W.J., 2000. A simple method for estimating frequency response corrections for eddy covariance systems. Agric. For. Meteorol. 104, 185–198.

Massman, W.J., 2001. Reply to comment by Rannik on "A simple method for estimating frequency response corrections for eddy covariance systems". Agric. For. Meteorol. 107, 247–251.

Melton, Forrest S., et al. "OpenET: Filling a critical data gap in water management for the western united states." *JAWRA Journal of the American Water Resources Association* (2021).

Metzger, Jutta, et al. "Dead Sea evaporation by eddy covariance measurements vs. aerodynamic, energy budget, Priestley–Taylor, and Penman estimates." *Hydrology and Earth System Sciences* 22.2 (2018): 1135-1155.

Miller, Scott D., et al. "Platform motion effects on measurements of turbulence and air–sea exchange over the open ocean." *Journal of Atmospheric and Oceanic Technology* 25.9 (2008): 1683-1694.

Mohseni, Omid, and Heinz G. Stefan. "Stream temperature/air temperature relationship: a physical interpretation." *Journal of hydrology* 218.3-4 (1999): 128-141.

Moreo, Michael T., and Amy Swancar. *Evaporation from Lake Mead, Nevada and Arizona, March 2010 through February 2012*. No. 2013-5229. US Geological Survey, 2013.

Mosner, Melinda S., and Brent T. Aulenbach. "Comparison of methods used to estimate lake evaporation for a water budget of Lake Seminole, southwestern Georgia and northwestern Florida." Georgia Institute of Technology, 2003.

Myers, Tom. "Loss rates from Lake Powell and their impact on management of the Colorado River." *JAWRA Journal of the American Water Resources Association* 49.5 (2013): 1213-1224.

Morton, Fred I. "Operational estimates of lake evaporation. "*J. of Hydrology*" 66.1-4 (1983): 77-100.

Payton, Elizabeth, Rebecca Smith, Carly Jerla, and James Prairie. 2020. "Primary Planning Tools." Chap. 3 in Colorado River Basin Climate and Hydrology: State of the Science, edited by J. Lukas and E. Payton, 82-111. Western Water Assessment, University of Colorado Boulder.

Quinn, F.H. 1979. An Improved Aerodynamic Evaporation Technique for Large Lakes with Application to the International Field Year for the Great Lakes. Water Resources Research, vol. 15, no. 4, pp. 935-940, 1979.

Bureau of Reclamation (Reclamation, 1986). Lake Powell evaporation numbers. Bureau of Reclamation Upper Colorado Regional Office.

Bureau of Reclamation (Reclamation, 2016). Improving Reservoir Evaporation Estimates. Science and Technology Program Research and Development Office ST-2012-7662-1.

Bureau of Reclamation (Reclamation, 2021). Deployment of the Collison Floating
    Evaporation Pan on Lake Powell, UT-AZ and Cochiti Lake, NM to
    Improve Evaporation Rate Measurement Accuracy and Precision. Science
    and Technology Program Research and Development Office ST-2018-
    8119-01.

Robinson, P. J., Davies, J. A. *Laboratory Determinations of Water Surface*
    Emissivity. Journal of Applied Meteorology **1972**, 11, 1391-1393.

Rouse, W. R., Oswald, C. J., Binyamin, J., Spence, C., Schertzer, W. M.,
    Blanken, P. D., Bussières, N., & Duguay, C. R. (2005). The Role of
    Northern Lakes in a Regional Energy Balance, Journal of
    Hydrometeorology, 6(3), 291-305. Retrieved Apr 7, 2022, from
    https://journals.ametsoc.org/view/journals/hydr/6/3/jhm421_1.xml

Rubin, D.B., (1987) Interval estimation from multiply-imputed data: A case study
    from using census agriculture industry codes, *Journal of Official Statistics*,
    3(4), 375-387.

Rubin, D.B., (1996) Multiple Imputation after 18+ Years, Journal of the
    American Statistical Association, 91:434, 473-489, DOI:
    10.1080/01621459.1996.10476908

Schenker, N. and Taylor, J.M.G., (1996) Partially parametric techniques for
    multiple imputation, Computational Statistics & Data Analysis, 22(4),
    425-446, https://doi.org/10.1016/0167-9473(95)00057-7.

Sellers, William D. *Physical climatology*. No. 551.6 S467. University of Chicago
    Press, 1965.

Singh, V. P., & Xu, C. Y. (1997). Evaluation and generalization of 13 mass-
    transfer equations for determining free water evaporation. *Hydrological*
    Processes, *11*(3), 311-323.

Spence, C., P.D. Blanken, N. Hedstrom, V. Fortin, and H. Wilson. "Evaporation
    from Lake Superior: 2 Spatial distribution and variability."*J. of Great*
    Lakes Research" 37. (2011): 717-724.

Subrahamanyam, D. B., & Ramachandran, R. (2002). Air–sea interface fluxes
    over the Indian Ocean during INDOEX, IFP-99. *Journal of atmospheric*
    and solar-terrestrial physics, *64*(3), 291-305.

Tanner, C.B., & Thurtell, G.W. (1969). ANEMOCLINOMETER
    MEASUREMENTS OF REYNOLDS STRESS AND HEAT
    TRANSPORT IN THE ATMOSPHERIC SURFACE LAYER.

Tanny, J., Cohen, S., Assouline, S., Lange, F., Grava, A., Berger, D., ... &
    Parlange, M. B. (2008). Evaporation from a small water reservoir: Direct
    measurements and estimates. *Journal of Hydrology*, *351*(1), 218-229.

Trask, James C., Graham E. Fogg, and Carlos E. Puente. "Resolving hydrologic
    water balances through a novel error analysis approach, with application
    to the Tahoe basin." *Journal of Hydrology* 546 (2017): 326-340.

van Buuren, S., K. Groothuis-Oudshoorn (2011). mice: Multivariate Imputation
    by Chained Equations in R. Journal of Statistical Software, 45(3), 1-67.
    URL https://www.jstatsoft.org/v45/i03/.

van Buuren, S. (2021). Package 'mice.' January 27, 2021. 188 pp.
https://amices.org/mice/. Accessed on April 7, 2021.

Verburg, P. and Antenucci, J. P. (2010). Persistent unstable atmospheric boundary
layer enhances sensible and latent heat loss in a tropical great lake: Lake
Tanganyika. *Journal of Geophysical Research: Atmospheres*, *115*(D11).

Vickers, D., & Mahrt, L. (1997). Quality Control and Flux Sampling Problems for
Tower and Aircraft Data, *Journal of Atmospheric and Oceanic
Technology*, *14*(3), 512-526. Retrieved Mar 23, 2022,
from https://journals.ametsoc.org/view/journals/atot/14/3/1520-
0426_1997_014_0512_qcafsp_2_0_co_2.xml

Webb, E.K., Pearman, G.I. and Leuning, R. (1980), Correction of flux
measurements for density effects due to heat and water vapour transfer.
Q.J.R. Meteorol. Soc., 106: 85-100.
https://doi.org/10.1002/qj.49710644707

Westerhoff, R. S. "Using uncertainty of Penman and Penman–Monteith methods
in combined satellite and ground-based evapotranspiration
estimates." *Remote Sensing of Environment* 169 (2015): 102-112.

Xia, Youlong, et al. "Continental-scale water and energy flux analysis and
validation for the North American Land Data Assimilation System project
phase 2 (NLDAS-2): 1. Intercomparison and application of model
products." *Journal of Geophysical Research: Atmospheres* 117.D3 (2012).

Xue, B. L., Komatsu, H., Kumagai, T., Kotani, A., Otsuki, K., & Ohta, T.
(2012). Interannual variation of evapotranspiration in an eastern Siberian
larch forest. *Hydrological Processes*, *26*(15), 2360-
2368. https://doi.org/10.1002/hyp.9195

Yonemura, S., Ono, K., Ikawa, H., Kim, W., Mano, M., & Miyata, A. (2017).
Comparison of fallow season CO2 efflux from paddy soil estimated using
laboratory incubation with eddy covariance-based flux. Journal of
Agricultural Meteorology, 73, 140-145.

Zhao, Gang, and Huilin Gao. "Estimating reservoir evaporation losses for the
United States: Fusing remote sensing and modeling approaches." *Remote
Sensing of Environment* 226 (2019): 109-124.

Zhao, Gang, et al. "Collection 6.1 MODIS Reservoir Product Algorithm
Theoretical Basis Document (ATBD) Version 1.0." *NASA GSFC* (2021).

Appendix 1.   Aerodynamic Mass Transfer Approach

Reservoir evaporation at each site was calculated following the aerodynamic mass transfer approach (Quinn, 1979; Subrahamanyam, 2002; Tanny 2008; Verburg and Antenucci, 2010). The mass-transfer aerodynamic evaporation code was originally developed in MATLAB under S&T 1512 and later translated to python by DRI (Spears, 2016). The AeroEvap python package developed by the DRI was utilized for all aerodynamic calculations.

The aerodynamic method estimates vapor flux based on differential specific humidity and turbulent transfer theory where

$$E = \rho_{mair} C_E u(q_{sat} - q_2) \times t_{step} \tag{1}$$

and E is evaporation (mm t_{step}^{-1}), t_{step} is a time step conversion (s $measurement\ t_{step}^{-1}$), ρ_{mair} is the density of moist air (kg m^{-3}), C_E is the bulk transfer coefficient (unitless), u is the windspeed at 2 m (m s^{-1}), q_2 is the specific humidity at 2 m (kg kg^{-1}), and q_{sat} is the saturated specific humidity at the water surface (kg kg^{-1}). The timestep conversion scales from an instantaneous flux rate (per second) to flux over the sampling period (30 minutes for this study). Note that vapor flux of kg m^{-2} is equivalent to mm assuming a water density of 1000 kg m^{-3} and length conversion of 1000 mm m^{-1}. C_E values for each reservoir were based on Monin-Obukhov Similarity Theory (MOST) following equations developed by Brutsaert, 1982 (see Bulk mass-transfer coefficient section below).

Saturated specific humidity at the water surface, q_{sat}, was calculated by

$$q_{sat} = \frac{0.622 e_{sat}}{P - 0.378 e_{sat}} \tag{2}$$

where e_{sat} (kPa) is the vapor pressure at the surface and P is atmospheric pressure (kPa) at the surface. Vapor pressure at the surface, e$_{sat}$, was calculated from the water surface skin temperature by

$$e_{sat} = 0.6108 e^{\frac{17.27 T_{skin}}{T_{skin} + 237.3}} \tag{4}$$

where T_{air} is the air temperature (°C), and T_{skin} is the skin temperature adjusted for both emissivity and reflected radiation (°C; see Skin Temperature Correction section below). The specific humidity at 2 m, q_2, was calculated using barometric pressure and vapor pressure

$$q_2 = \frac{.622e_2}{P - .378e_2} \tag{5}$$

where e_2 (kPa) is the saturated vapor pressure at 2 m, found using steps similar to equations 2 and 4 above. The density of moist air, ρ_{mair}, was calculated according to (Brutsaert, 2005)

$$\rho_{mair} = \frac{P}{R_a T_{air}(1 + .61q_2)} \tag{6}$$

where P is the atmospheric pressure (Pa), R_a is the universal gas constant (286.9 J kg^{-1} K^{-1}), and T_{air} is the air temperature (K).

Bulk mass-transfer coefficient, C$_E$

The bulk mass-transfer coefficient, C$_E$, was calculated for each time-step using an iterative approach based on MOST. MOST applies stability corrections to the near surface transfer coefficients based on wind speed and atmospheric stability. The Monin-Obukhov length, L (see equation 9), can be used to describe atmospheric stability where, $\frac{z}{L} = 0$, $\frac{z}{L} > 0$, and $\frac{z}{L} < 0$ correspond to neutral, stable, and unstable conditions, respectively.

The iterative process relies on values of surface temperature, air temperature, wind speed, atmospheric pressure, and specific humidity. This iterative approach has been applied in various forms to estimate bulk transfer coefficients over water bodies including both oceans and reservoirs (Quinn, 1979; Croley, 1989; Tanny, 2008; Verburg, 2010; Subrahamanyam, 2002). This study follows stability functions and roughness length equations developed by Brutsaert, 1982. The general approach is presented below:

Friction velocity, u^*, can be solved by

$$u^* = \frac{u\,k}{\ln\left(\frac{z}{z_0}\right) - \Psi_m} \tag{7}$$

where u is average wind speed at the reference height (m s^{-1}), k is von Karman's constant (0.41), z is the measurement height (2 m in this study), z_0 is the roughness length of momentum (m; estimated below), and Ψ_m is the stability function of momentum. Stability parameters Ψ_m (wind/momentum) and Ψ_v (humidity) are solved for based on atmospheric stability as follows:

Neutral Conditions (z/L=0)

$$\Psi_m = \Psi_v = \Psi_t = 0 \tag{8a}$$

Stable Conditions (z/L $\geq$ 0)

56

$$\Psi_m = \Psi_v = \Psi_t = \frac{-5.2\,Z}{L} \tag{8b}$$

Unstable Conditions ($z/L \leq 0$)

$$\Psi_m = 2\ln\left(\frac{[1+x]}{2}\right) + \ln\left(\frac{[1+x^2]}{2}\right) - 2\tan^{-1}(x) + \frac{\pi}{2} \tag{8c}$$

$$\Psi_v = \Psi_t = 2\ln\left[\frac{(1+x^2)}{2}\right]$$

where $x = \left(1 - 16\,(z/L)\right)^{\frac{1}{4}}$. The Monin-Obukhov length, L, can be represented by

$$L = \frac{T_v\,u^{*2}}{g\,K\,\theta^*}, \tag{9}$$

where T_v is the virtual temperature of the atmosphere, θ^* is the scaling parameter for temperature (Quinn, 1979; Subrahamanyam, 2002), g is the acceleration due to gravity (9.8 m s^{-2}). T_v can be solved by

$$T_v = T_{air}(1 + 0.61q_{air})$$

and θ^* can be solved by

$$\theta^* = [K(\theta_2 - \theta_0)]/\left[\ln\left(\frac{Z}{Z_{ot}}\right) - \Psi_t\right] \tag{10}$$

where θ_2 is the potential air temperature at 2 m, θ_0 is the potential temperature at the water surface, and z_{ot} is roughness length of temperature. The roughness length of momentum was estimated by

$$z_0 = \frac{\alpha\,u^{*2}}{g} + \frac{0.11v}{u^*} \tag{11}$$

Where v is the kinematic viscosity,

$$v = \frac{4.94\times10^{-8}T_{air} + 1.7185\times10^{-5}}{\rho_{mair}}.$$

The roughness length of humidity, z_v, is assumed to be equal to the roughness length of temperature and was estimated by

$$z_v = z_{ot} = 7.4\exp\left(-2.25(z_0u^*)^{.25}\right) \tag{12}$$

The above system of equations can be solved iteratively starting with equations 11, 12, and 10 using the initial conditions of u^*=0.1 m s^{-1}, and Ψ_m and Ψ_v = 0. The iteration then continues solving equations 9, 8, 10, 11, 12, and 7 until the values converge. The final values are used to solve for C_E by

$$C_E = \frac{k^2}{\left[\ln\left(\frac{Z}{Z_0}\right)-\Psi_m\right]\left[\ln\left(\frac{Z}{Z_v}\right)-\Psi_v\right]}$$

This final C_E value can be used in equation 1 to solve for evaporation.

Skin Temperature Correction, T$_s$

Following the approach for correcting skin temperature given by Apogee Instruments (2015), the longwave radiation measured by the IRT can be expressed as

$$LW_{sensor} = \varepsilon LW_{water} + (1-\varepsilon)LW_{in} \tag{13}$$

where LW_{sensor} (W m^{-2}) is the outgoing longwave radiation measured by the sensor, LW_{water} (W m^{-2}) is the outgoing longwave radiation emitted by the water, and LW_{in} (W m^{-2}) is the incoming longwave radiation. Equation 13 can then be reduced using the Stephan-Boltzman equation to the form

$$\sigma T_{uncorr}^4 = \varepsilon\sigma T_{corr}^4 + (1-\varepsilon)\sigma T_{sky}^4 \tag{14}$$

where T_{uncorr} (K) is the uncorrected skin temperature reading from the sensor, T_{corr} (K) is the corrected skin temperature, T_{sky} (K) is the background sky temperature, ε is the emissivity of the water, and σ is the Stephan-Boltzmann constant, $5.670 \times 10^{-8}\frac{W}{m^2}K^4$. In this study, the IRT was positioned at approximately 45° to the normal, therefore an emissivity of 0.97 was assumed based on findings by Robinson and Davies (1972). The corrected skin temperature can be found by rearranging equation 14 to

$$T_{corr} = \sqrt[4]{\frac{T_{uncorr}^4-(1-\varepsilon)T_{sky}^4}{\varepsilon}}. \tag{15}$$

Using the Stephan-Boltzman equation, the background temperature of the sky can be expressed as

$$LW_{in} = \sigma T_{sky}^4 \tag{16}$$

where LW_{in} (W m^{-2}) is the incoming longwave radiation measured with the upward facing sensors of the CNR4 pyrgeometer. Equation 16 can be rearranged to estimate T_{sky}^4 as

$$T_{sky}^4 = \frac{LW_{in}}{\sigma}. \tag{17}$$

Substituting equation 17 into equation 15 gives

58

$$T_{corr} = \sqrt[4]{\frac{T_{uncorr}^4 - \frac{(1-\varepsilon)LW_{in}}{\sigma}}{\varepsilon}} \quad . \tag{18}$$

Appendix 2.   Thirty-Minute Evaporation Data

Appendix 2.1   Eddy Covariance

Appendix 2.1.1   Platform Motion

Figure 23 shows scatterplots of 30-minute average wind components (u, v, and w) of motion-uncorrected (i.e., observed) and motion-corrected time series at Padre Bay and Warm Creek Bay over the study period. Results indicate that motion-corrected horizontal winds (the u- and v-wind components) are nearly identical to corresponding motion-uncorrected winds (u- and v-components). However, there are differences in the vertical (w) wind component between the two datasets at each platform. One possible reason why w-component corrected wind speeds are different from w-component measured wind speeds is that surface waves mostly induce vertical platform motion (not horizontal). A second possible reason is that the anchoring system installed at both platforms reduces platform accelerations in the east/west and north/south directions but does not reduce platform accelerations in the vertical direction. Stated differently, the anchoring systems attached to both platforms inhibited lateral accelerations but did not inhibit vertical accelerations. The percent difference (computed as motion-corrected wind component minus observed component relative to motion-corrected wind component) averaged over the study period for each site is shown in Table 8.1. Large differences in the vertical component at Warm Creek Bay may be related to enhanced boat activity and/or the mounting of the CFEP to the platform. The differences in vertical wind speed have a very small impact on the 3D wind speed between the two datasets.
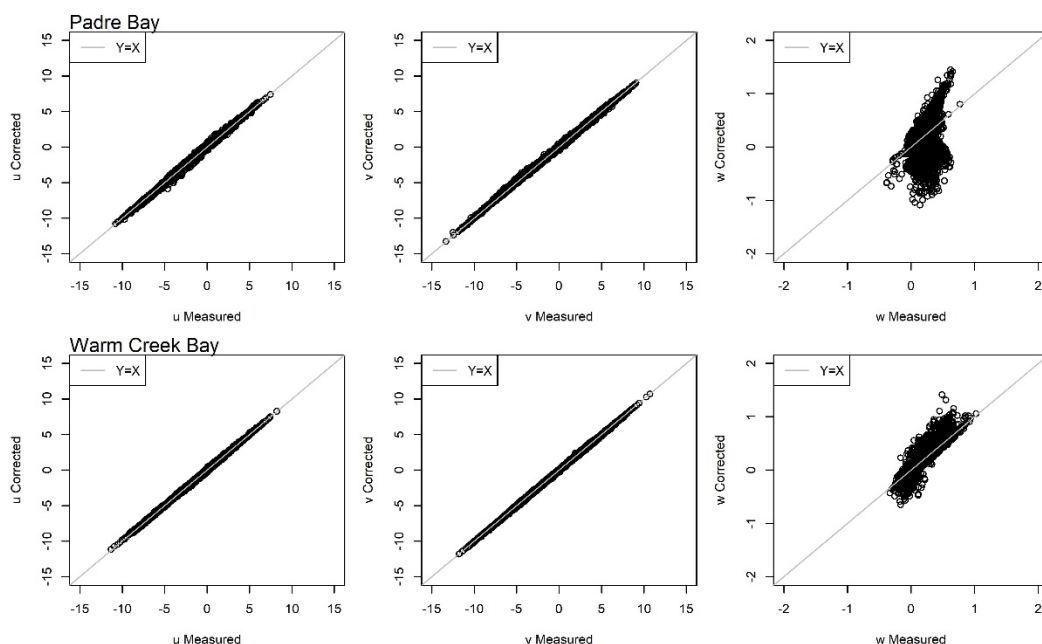
Figure 23—Scatterplots of 30-minute average (left) u-corrected versus u-measured, (middle) v-corrected versus v-measured, and (right) w-corrected versus w-measured wind components (m/s) at (top) Padre Bay and (bottom) Warm Creek Bay over the study period.

Table 8.1—Percent difference in individual wind component speeds (u, v, and w) between motion-corrected and measured variables at Padre Bay and Warm Creek Bay over the study period.

Component of Total Wind Vector	Percent Difference (Corrected minus Measured)	
	Padre Bay	**Warm Creek Bay**
u (zonal)	6.1	-0.1
v (meridional)	0.6	1.6
w (vertical)	-5.5	-53.6

To understand the impacts of correcting for platform motion on evaporation totals at Padre Bay and Warm Creek Bay based on the EC method, we present scatterplots of evaporation totals computed using motion-corrected winds versus evaporation totals computed using motion-uncorrected winds (i.e., observed winds). Results at the 30-min time scale are shown in Figure 24. Scatterplots (top panels of Figure 24) indicate that motion-corrected, and motion-uncorrected evaporation estimates are highly correlated (r=0.94 and 0.96 at Padre Bay and Warm Creek Bay, respectively) with little bias (slope=0.87 and 0.93 at Padre Bay and Warm Creek Bay, respectively, when forced through the intercept), and that agreement between these datasets is stronger at the Warm Creek Bay location.

62

Box and whisker plots are shown in the bottom four panels of Figure 24, which summarize differences in the motion-corrected and motion-uncorrected estimates as a function of month. Thick horizontal lines in the box and whisker plots represent the population median, shaded rectangles extend to the 25th and 75th percentiles, and whiskers extend to 1.5 times the inter-quartile range. Outliers are not shown in order to emphasize median conditions. Percent differences between motion-corrected and motion-uncorrected 30-min evaporation totals (relative to motion-corrected) at Padre Bay and Warm Creek Bay are shown in the bottom row of Figure 24. Approximately 96.5% and 96.6% of the differences in 30-min motion-corrected and motion-uncorrected values are between -100% and +100% and at Padre Bay and Warm Creek Bay, respectively.
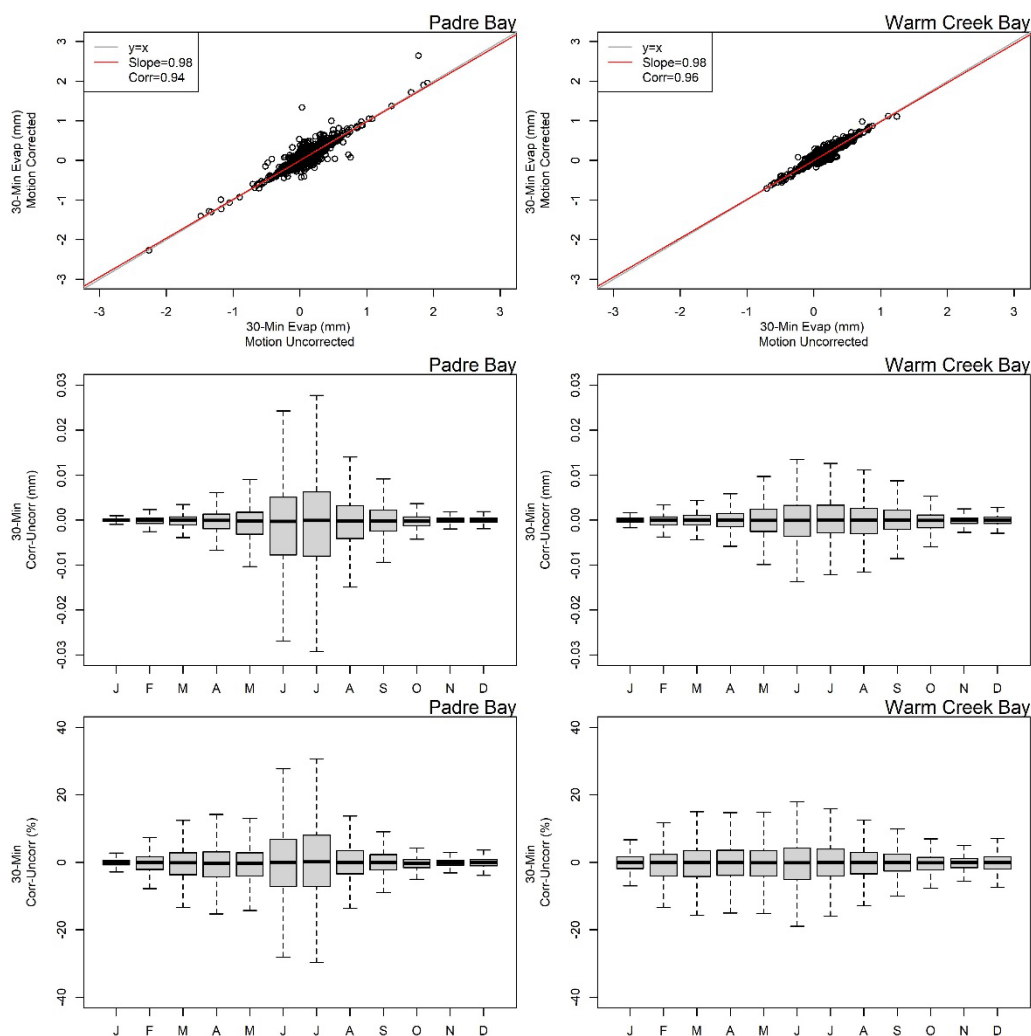
Figure 24—(top row) Scatterplots of 30-min motion corrected evaporation rates (mm) versus 30-min motion uncorrected evaporation rates (mm). Slope values represent the slope of a linear model when forced through the intercept (0,0). (middle and bottom rows) Box and whisker plots of difference between 30-min estimates (corrected minus uncorrected) as a function of month of year at (left) Padre Bay and (right) Warm Creek Bay expressed in mm and %, respecitvely. Whiskers in the boxplots extend to 1.5 times the inter-quartile range.

Results in the bottom four panels of Figure 24 indicate that median differences between 30-min motion corrected and motion uncorrected evaporation estimates differ between the two locations, though there is a clear seasonal component at both. For instance, the range of observed differences is larger during summer months at Padre Bay than Warm Creek Bay. This is reflected in both plots expressed as mm and percent. At Padre Bay, the largest positive median differences (expressed as a percent) occur during June and July, while the largest

64

negative median differences occur May and October. At Warm Creek Bay, all median differences (expressed as a percent) are negative, with the largest negative median difference in May.

Scatterplots and box and whisker plots demonstrating differences between motion-corrected and motion-uncorrected evaporation estimates at the daily time scale are shown in Figure 25. As with the 30-min estimates, the daily totals at both sites show strong agreement (correlation of 0.99 and 1 at Padre Bay and Warm Creek Bay, respectively). Daily totals reach almost 15 mm at both sites (14.65 mm from motion-uncorrected estimates at Padre Bay and 15.99 mm from motion-corrected estimates at Warm Creek Bay). As with the 30-min data, monthly differences (mm) in the datasets at Padre Bay show a more pronounced seasonal cycle, with the largest range in differences observed during June, July, and August again. Differences between the datasets at Warm Creek Bay show variations throughout the year, though monthly differences show less variability than with the 30-min datasets. The seasonal cycle of percent differences at Warm Creek Bay is out of sync with percent differences at Padre Bay. More specifically, the largest median percent differences at Warm Creek Bay occur during cool season months.
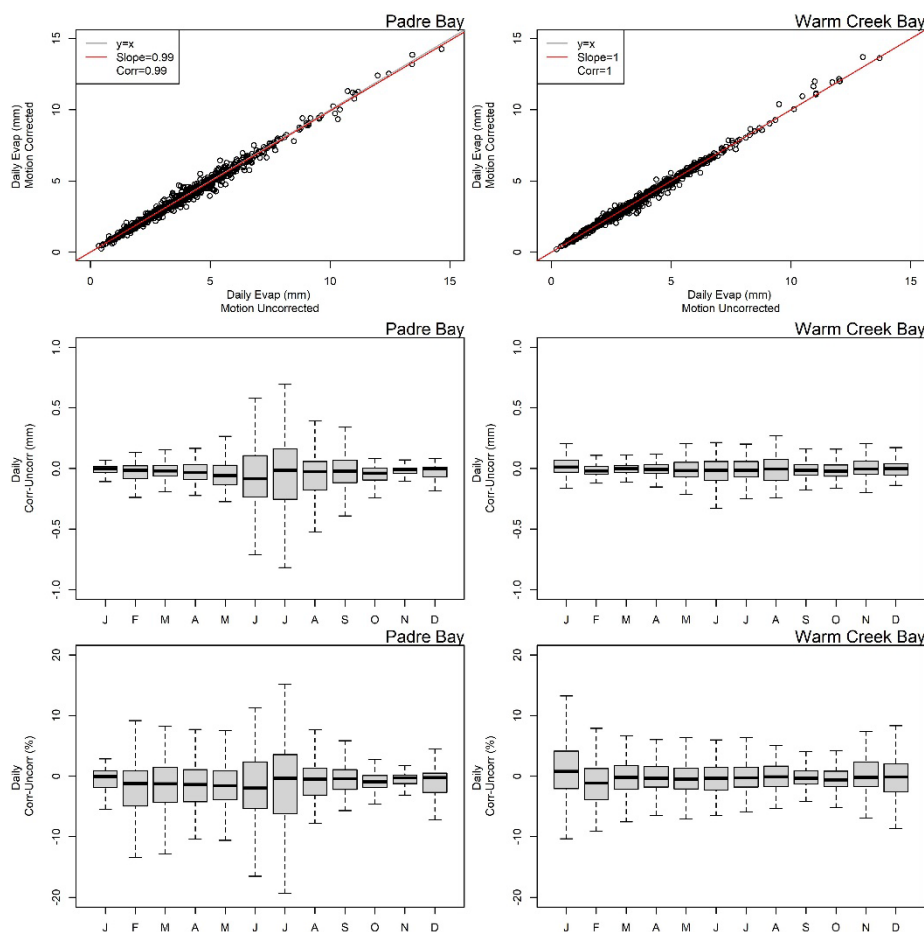
Figure 25—Same as Figure 24 except with at the daily time scale.

Differences in 30-min evaporation totals between the motion-corrected and motion-uncorrected estimates have a minimum impact on annual totals. For example, at Padre Bay, the annual difference ranges from -16.5 mm to -0.61 mm, while at Warm Creek Bay, the annual difference ranges from -6.48 mm to 1.16 mm (corrected minus uncorrected). Relative to motion-corrected totals, these differences reach at most 1% and 3% at Padre Bay and Warm Creek Bay, respectively.

Appendix 2.1.2   Gap Filling
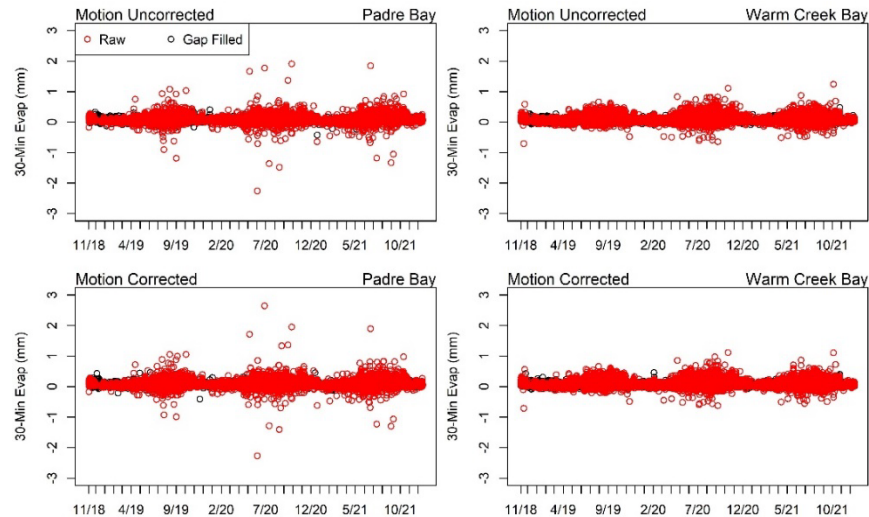
Figure 26—Raw and gap filled time series of 30-min average evaporation rates (mm) at (left) Padre Bay and (right) Warm Creek Bay based on the EC method.

Figure 27—Scatterplots of daily gap filled evaporation rates (mm) versus daily raw evaporation rates (mm) at (left) Padre Bay and (right) Warm Creek Bay based on the EC method. Y-axis values represent 24-hour totals, while x-axis values represent totals valid for less than 24 hours (due to missing values).

Appendix 2.1.3   30-Min Evaporation Estimates

Time series of 30-min evaporation totals at Padre Bay and Warm Creek Bay are shown in the top panels of Figure 28. Box-and-whisker plots of 30-min evaporation totals as a function of month are shown in the bottom panels, where box-and-whisker features are defined in the same manner as above (e.g., the thick horizontal line represents the median, the shaded rectangles extend to the 25th and 75th percentiles, and the whiskers extend to 1.5 times the inter-quartile range). Time series in the top two panels indicate that 30-min evaporation totals encompass positive and negative values at both locations. The box-and-whisker plots in the bottom two panels of Figure 28 demonstrate the variability in 30-min evaporation totals as a function of month. Median totals at both locations peak during July, August, and September, while median totals are lowest during January, February, and March. While both sites show similar monthly variability, median totals at Padre Bay are larger than the corresponding median totals at Warm Creek Bay during every month of the year.

Figure 28—(top) Time series and (bottom) monthly box and whisker plots of 30-min evaporation rates (mm) from the EC method at (left) Padre Bay and (right) Warm Creek Bay.

Appendix 2.2   Aerodynamic

Appendix 2.2.1 Gap Filling
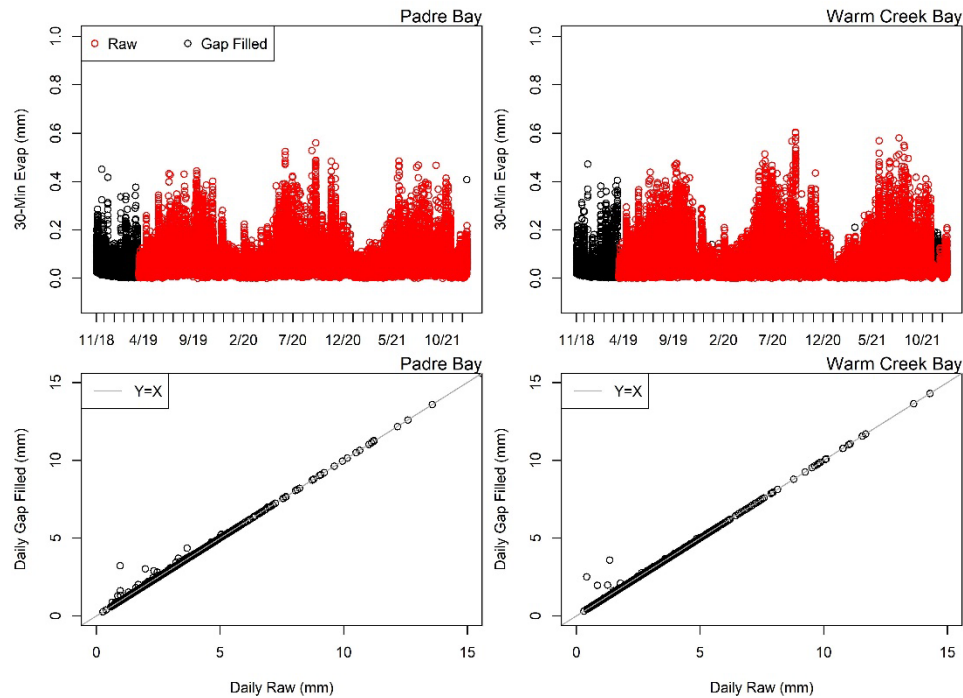
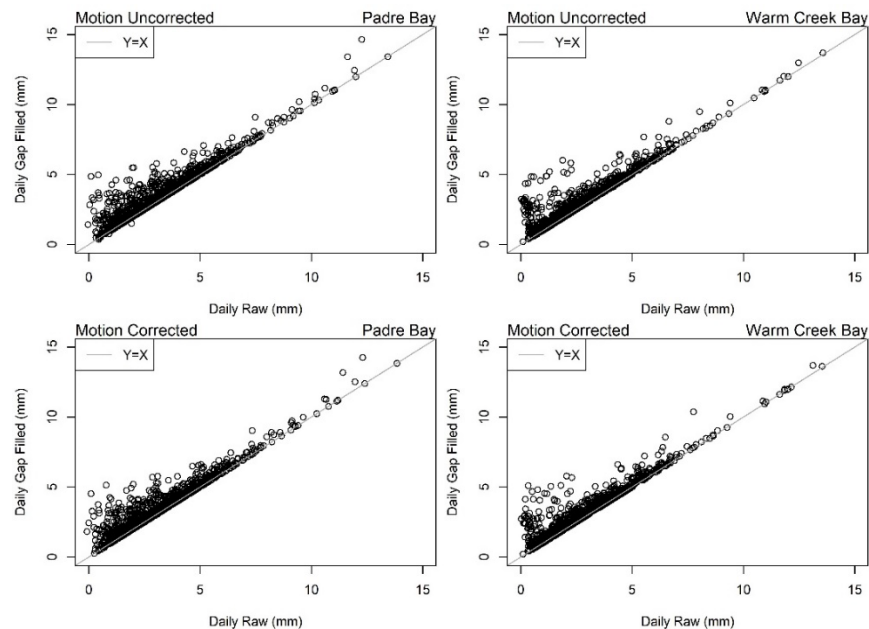**Figure 29—(top row) Raw and gap filled time series of 30-minute average evaporation rates (mm) and (bottom row) scatterplots of daily gap filled evaporation rates (mm) versus daily raw evaporation rates (mm) at (left column) Padre Bay and (right column) Warm Creek Bay. Y-axis values represent 24-hour totals, while x-axis values represent totals valid for less than 24 hours (due to missing values).**

Appendix 2.2.2 30-Min Evaporation Estimates

Figure 30 shows time series and box-and-whisker plots of 30-min evaporation totals computed using the aerodynamic method. Characteristics of the box-and-whisker plots are the same as previous definitions. The top two panels of the figure show that 30-min totals are relatively similar between the two locations. Both sites show a hard lower-limit near 0 mm, with a maximum 30-min total near 0.6 mm. Monthly variability in median 30-min totals differs between the two locations. The median 30-min total at Padre Bay peaks during October, with August ranked second and September ranked third. At Warm Creek Bay, the median 30-min total peaks during August, with July ranked second and September ranked third. This finding suggests that 30-min aerodynamic totals peak later in the season at Padre Bay compared with Warm Creek Bay. Median totals at Padre Bay reach a minimum in March, whereas at Warm Creek Bay, median totals reach a minimum in January.
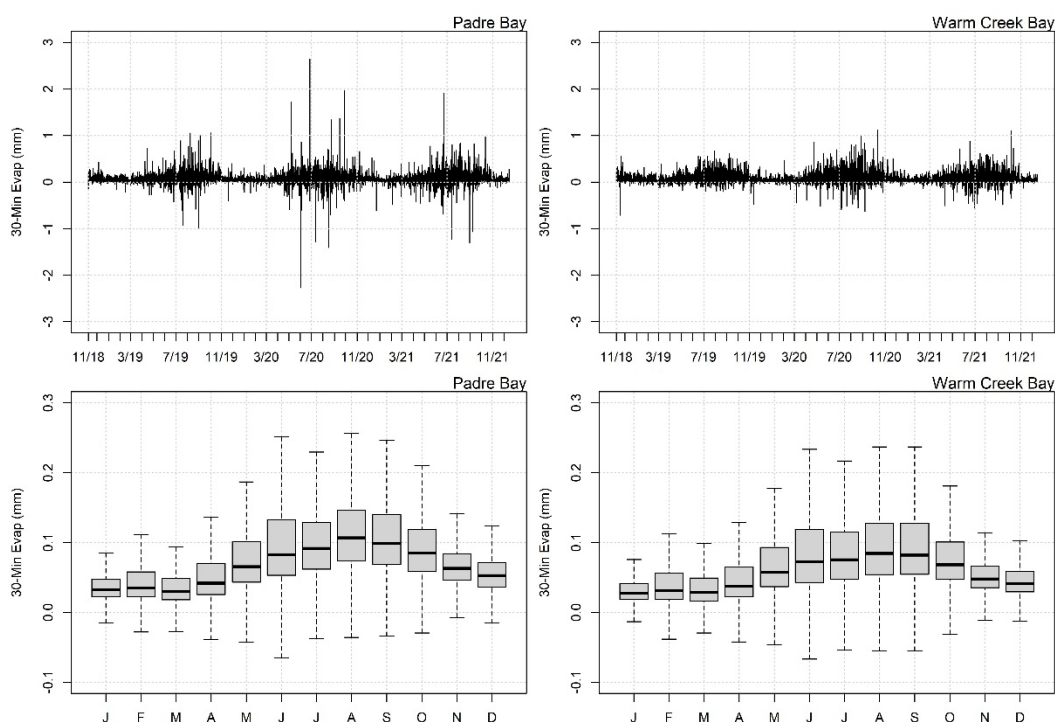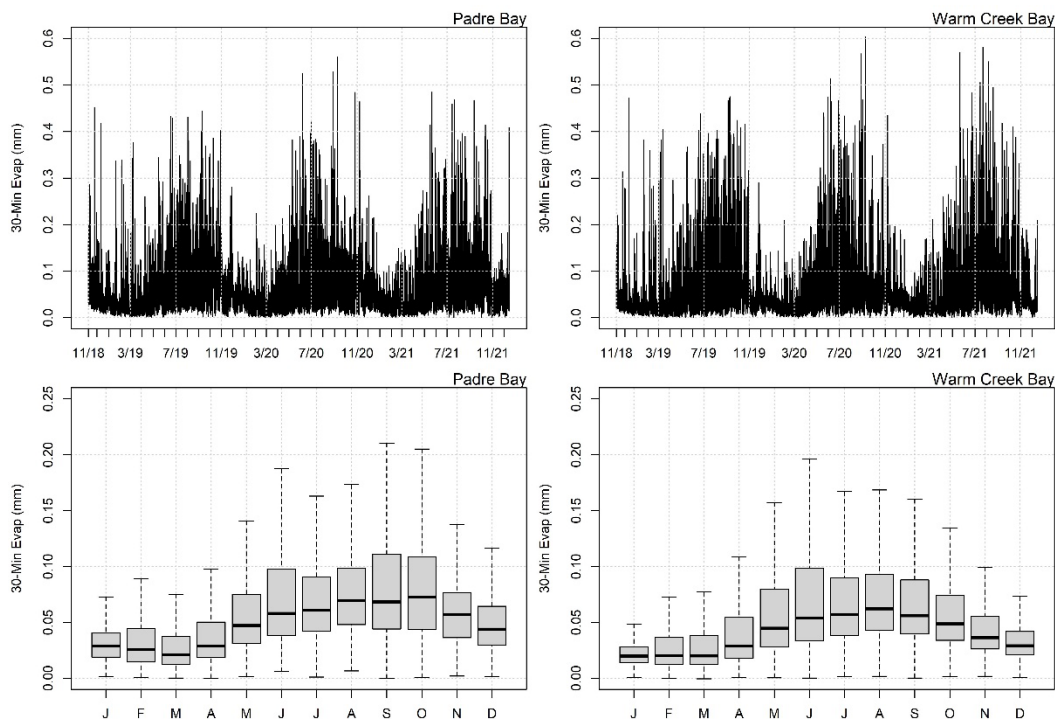
Figure 30—(top) Time series and (bottom) monthly box and whisker plots of 30-min evaporation totals (mm) from the aerodynamic method at (left) Padre Bay and (right) Warm Creek Bay.

Appendix 2.3   Method Comparisons

Scatterplots in Figure 12 show EC evaporation totals versus corresponding aerodynamic evaporation totals at Padre Bay and Warm Creek Bay at the 30-min time scale. Correlations between the two 30-min datasets are 0.61 and 0.64 at Padre Bay and Warm Creek Bay, respectively. The weaker correlations with the 30-min data (relative to daily totals in the section 4.1.1) appear related to behavior at low aerodynamic totals. More specifically, 30-min EC estimates at Padre Bay show larger variability (i.e., ± 3 mm) when the 30-min aerodynamic estimates are less than 0.1 mm. This finding suggests that the two methods show less agreement during periods of low evaporation (as estimated by the aerodynamic method). Similar results are shown at Warm Creek Bay, albeit with a smaller range in 30-min EC estimates (i.e., ± 1 mm).
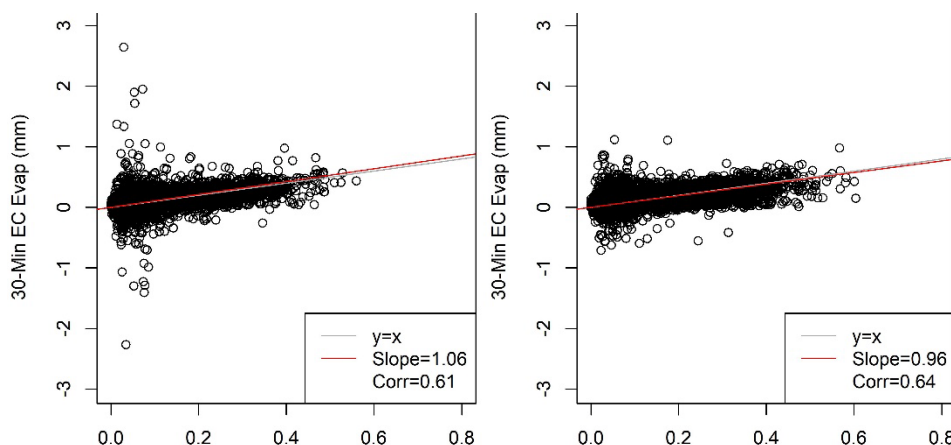
Figure 31—Scatterplots of evaporation totals (mm) from the eddy covariance method versus the aerodynamic method at 30-min time scales at (left) Padre Bay and (right) Warm Creek Bay. Slope values represent the slope of a linear model when forced through the intercept (0,0). In some instances, the y=x line is under the linear model forced through the intercept.

Appendix 2.3.1 Comparison Metrics

We computed four metrics commonly used to summarize relationships between observed and modeled data. We treated EC data as observed and aerodynamic data as modeled. The metrics include correlation (r), root mean squared error (RMSE), mean absolute error (MAE), and slope. The correlation coefficient between both datasets was computed using the Pearson product moment coefficient of linear correlation. The RMSE was computed as the square root of the average of the squared differences between the modeled and observed values. The MAE was computed as the arithmetic average of the absolute values of the differences between each pair of observed and modeled data. The RMSE is more sensitive to outliers than MAE (Wilks, 2019). Metrics based on 30-min and daily observations at Padre Bay are listed in Table 8.2. Analogous values for Warm Creek Bay are listed in
Table 8.3.

Table 8.2—Basic statistical metrics that describe the relationship between monthly EC and aerodynamic evaporation estimates at Padre Bay. r represents correlation. RMSE (mm) and MAE (mm) are computed by treating EC estimates as "observed" and aerodynamic estimates as "modeled". Slope through origin represents the slope of a linear regression model fit to the monthly data (EC versus aerodynamic) while forcing the y-intercept to 0.

Month	30-Minute Data				Daily Data			
	r	RMSE (mm)	MAE (mm)	Slope thru Origin	r	RMSE (mm)	MAE (mm)	Slope thru Origin
January	0.61	0.02	0.01	0.77	0.88	0.39	0.29	0.89
February	0.54	0.03	0.02	0.69	0.75	0.82	0.59	0.81
March	0.54	0.03	0.02	0.67	0.79	0.59	0.45	0.82
April	0.55	0.04	0.03	0.62	0.88	0.66	0.56	0.83
May	0.64	0.06	0.04	0.67	0.93	0.94	0.79	0.85
June	0.47	0.1	0.05	0.53	0.88	1.33	1.06	0.82
July	0.41	0.08	0.05	0.54	0.68	1.37	1.21	0.75
August	0.41	0.09	0.06	0.51	0.79	1.77	1.61	0.7
September	0.63	0.07	0.04	0.67	0.94	1.43	1.26	0.82
October	0.76	0.04	0.03	0.83	0.95	0.84	0.71	0.90
November	0.71	0.03	0.02	0.85	0.91	0.66	0.48	0.91
December	0.52	0.03	0.02	0.77	0.75	0.73	0.47	0.87

Table 8.3—Same as Table 8.2 except valid for EC and aerodynamic evaporation estimates valid at Warm Creek Bay.

Month	30-Minute Data				Daily Data			
	r	RMSE (mm)	MAE (mm)	Slope thru Origin	r	RMSE (mm)	MAE (mm)	Slope thru Origin
January	0.47	0.03	0.02	0.62	0.72	0.67	0.82	0.75
February	0.52	0.04	0.02	0.68	0.75	0.92	0.63	0.81
March	0.51	0.04	0.02	0.76	0.73	0.85	0.52	0.94
April	0.56	0.04	0.03	0.69	0.74	0.85	0.58	0.92
May	0.68	0.06	0.04	0.78	0.95	0.74	0.57	0.95
June	0.58	0.08	0.05	0.72	0.88	1.21	0.84	0.94
July	0.47	0.08	0.05	0.64	0.79	0.95	0.76	0.85
August	0.59	0.08	0.05	0.63	0.88	1.19	0.96	0.80
September	0.67	0.07	0.05	0.73	0.94	1.29	1.10	0.85
October	0.69	0.06	0.03	0.70	0.92	1.13	0.95	0.81
November	0.59	0.04	0.02	0.73	0.83	0.87	0.75	0.86
December	0.46	0.03	0.02	0.67	0.68	0.86	0.63	0.76

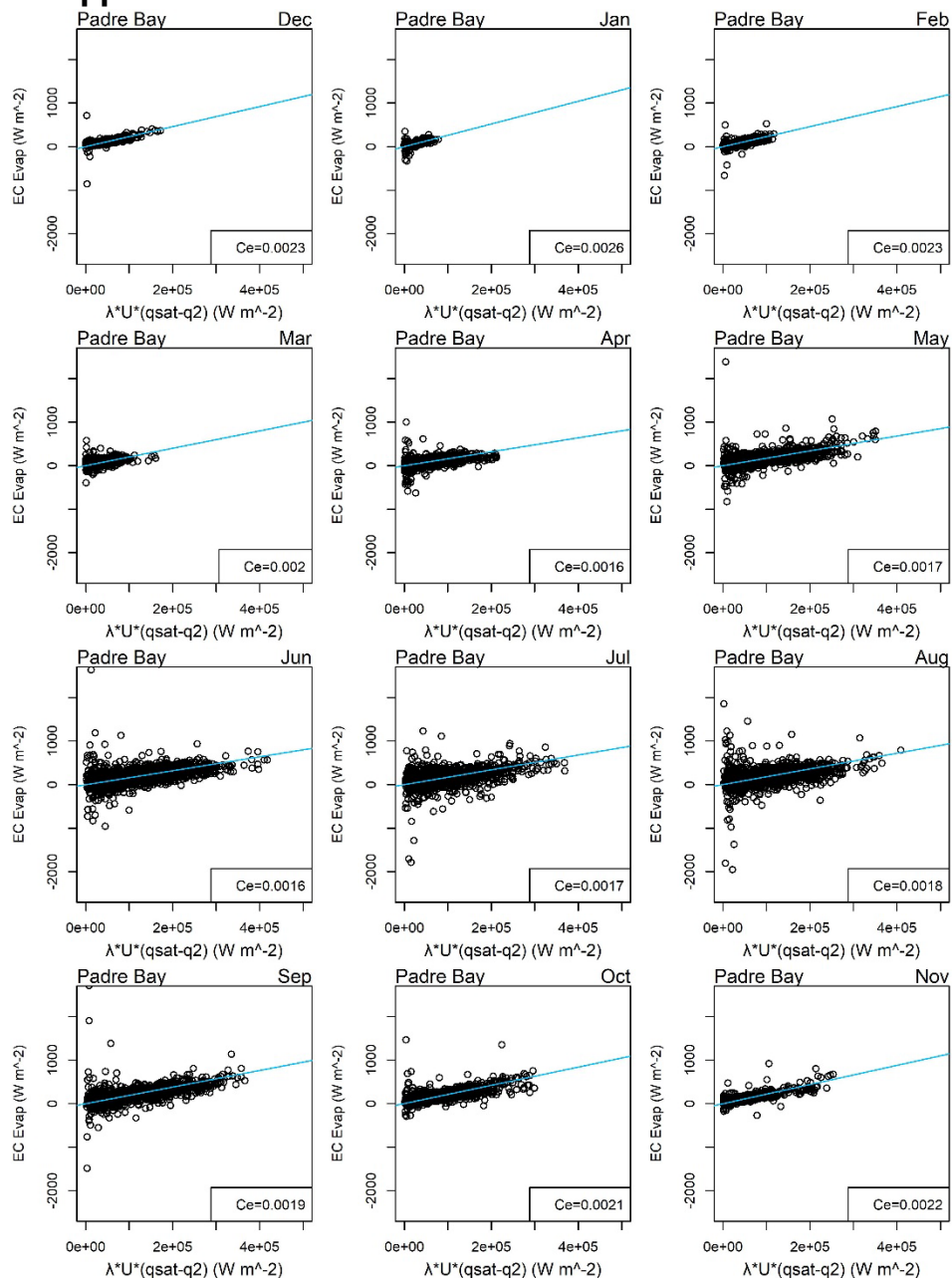## Appendix 2.3.2 Mass Transfer Coefficient Estimates

Figure 32—Scatterplots of EC latent heat flux (W m^{-2}) versus the product of the latent heat of vaporization, wind speed, and difference between saturated specific humidity and specific humidity at 2 m (W m^{-2}; all 30-min time step) at Padre Bay as a function of month of year.
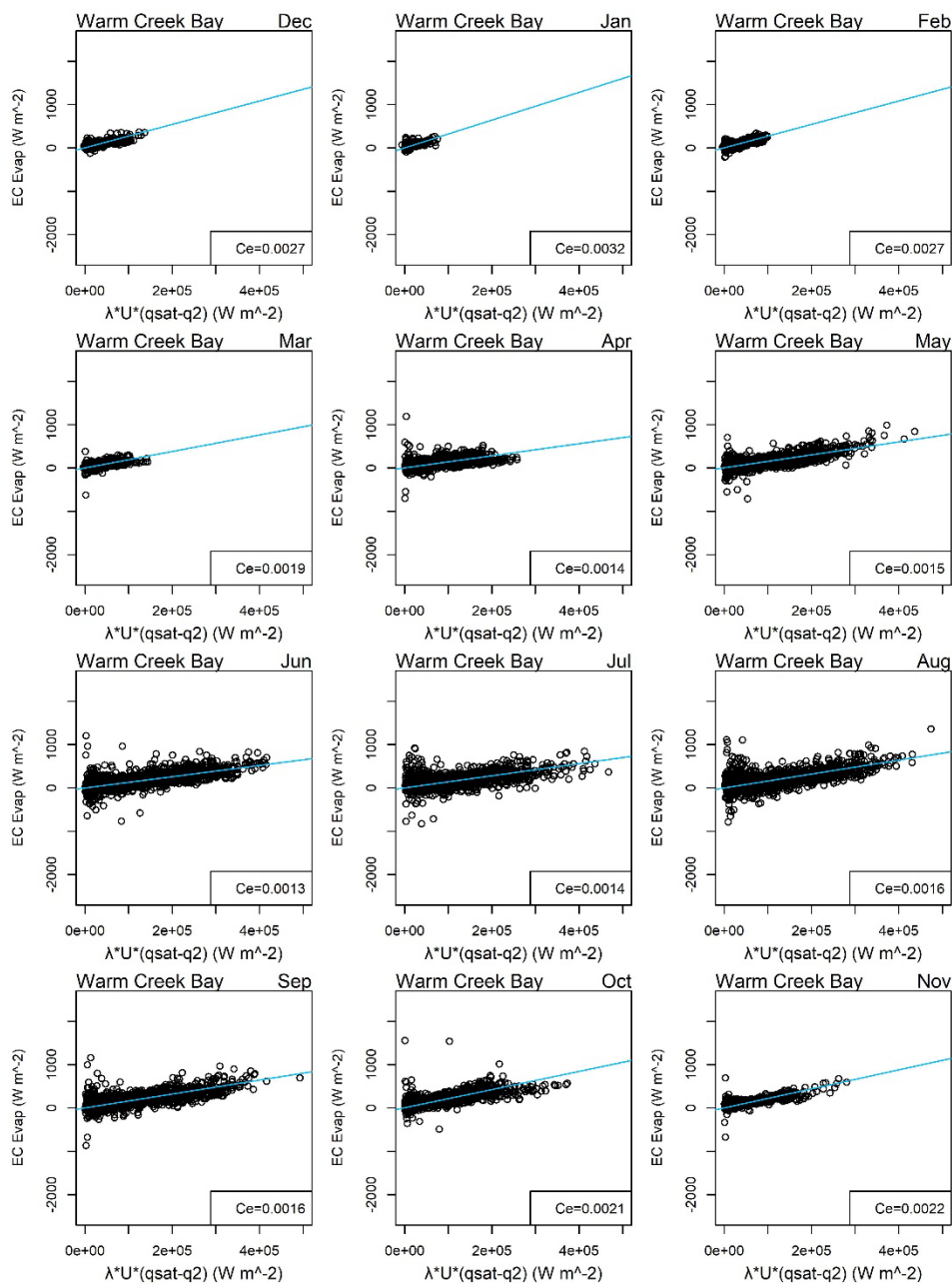
Figure 33—Same as Figure 32 except for Warm Creek Bay.

Appendix 3. Monthly Evaporation Totals

Table 8.4—Monthly evaporation totals (mm) at Padre Bay and Warm Creek Bay based on the two in-situ methods applied in the current study. Aerodynamic estimates are based on the standard method (i.e., not the alterative, adjusted Ce estimates).

Year	Month	EC Padre Bay	Aerodynamic Padre Bay	EC Warm Creek Bay	Aerodynamic Warm Creek Bay
2018	11	87.54	74.5	73.52	47.97
2018	12	91.47	65.35	81.99	49.68
2019	1	52.49	47.39	56.68	39.14
2019	2	59.26	51.52	64.84	52.21
2019	3	51.57	45.18	45.01	53.17
2019	4	63.93	49.94	60.36	56.98
2019	5	99.5	87.4	94.5	82.67
2019	6	122.9	95.47	122.41	92.85
2019	7	142.43	111.7	126.65	106.51
2019	8	162.89	114.5	142.87	115.35
2019	9	175.85	147.3	166.05	143.89
2019	10	160.25	139.94	135.02	110.74
2019	11	96.2	88.31	76.46	62.59
2019	12	77.97	70.73	60.37	52.88
2020	1	60.25	51.06	46.09	36.13
2020	2	62.41	51.08	56.77	42.58
2020	3	53.13	40.25	52.48	43.3
2020	4	76.98	60.58	75.6	61.93
2020	5	127.75	100.62	122.67	111.72
2020	6	157.36	138.16	142.05	144.53
2020	7	142.95	109.08	137.73	111.63
2020	8	164.55	122.88	161.49	124.7
2020	9	160.18	122.5	139.96	110.91
2020	10	143.6	117.24	131.65	96.93
2020	11	111.64	104.51	93.2	80.8
2020	12	92.18	86	73.28	62.08
2021	1	54.57	48.31	47.71	34.59
2021	2	54.91	41.66	48.21	41.55
2021	3	57.22	47.25	64.78	52.43

2021	4	79.89	69.31	78.88	76.86
2021	5	125.83	103.59	115.67	110.64
2021	6	148.2	114.76	134.48	124.51
2021	7	153.91	113.33	134.04	125.28
2021	8	182.16	122.89	148.27	126.33
2021	9	153.6	113.6	132.09	99.16
2021	10	130.32	124.04	116.06	95.59
2021	11	84.75	75.88	67.76	72.66
2021	12	40.1	42.14	32.62	24.89

Table 8.5—Monthly evaporation totals (ft) at Padre Bay and Warm Creek Bay based on the two in-situ methods applied in the current study. Aerodynamic estimates are based on the standard method (i.e., not the alterative, adjusted Ce estimates).

Year	Month	EC Padre Bay	Aerodynamic Padre Bay	EC Warm Creek Bay	Aerodynamic Warm Creek Bay
2018	11	0.29	0.24	0.24	0.16
2018	12	0.3	0.21	0.27	0.16
2019	1	0.17	0.16	0.19	0.13
2019	2	0.19	0.17	0.21	0.17
2019	3	0.17	0.15	0.15	0.17
2019	4	0.21	0.16	0.2	0.19
2019	5	0.33	0.29	0.31	0.27
2019	6	0.4	0.31	0.4	0.3
2019	7	0.47	0.37	0.42	0.35
2019	8	0.53	0.38	0.47	0.38
2019	9	0.58	0.48	0.54	0.47
2019	10	0.53	0.46	0.44	0.36
2019	11	0.32	0.29	0.25	0.21
2019	12	0.26	0.23	0.2	0.17
2020	1	0.2	0.17	0.15	0.12
2020	2	0.2	0.17	0.19	0.14
2020	3	0.17	0.13	0.17	0.14
2020	4	0.25	0.2	0.25	0.2
2020	5	0.42	0.33	0.4	0.37
2020	6	0.52	0.45	0.47	0.47
2020	7	0.47	0.36	0.45	0.37
2020	8	0.54	0.4	0.53	0.41
2020	9	0.53	0.4	0.46	0.36

2020	10	0.47	0.38	0.43	0.32
2020	11	0.37	0.34	0.31	0.27
2020	12	0.3	0.28	0.24	0.2
2021	1	0.18	0.16	0.16	0.11
2021	2	0.18	0.14	0.16	0.14
2021	3	0.19	0.16	0.21	0.17
2021	4	0.26	0.23	0.26	0.25
2021	5	0.41	0.34	0.38	0.36
2021	6	0.49	0.38	0.44	0.41
2021	7	0.5	0.37	0.44	0.41
2021	8	0.6	0.4	0.49	0.41
2021	9	0.5	0.37	0.43	0.33
2021	10	0.43	0.41	0.38	0.31
2021	11	0.28	0.25	0.22	0.24
2021	12	0.13	0.14	0.11	0.08